Science and Technology Facilities Council

Technical Report
STFC-TR-2026-018

Variations in ISIS target plate thermal conductivity from mining ISIS machine databases

DJS Findlay, M Romanovschi,
GD Howells, D Wilcox, SD Gallimore

August 2026

Enquiries concerning this report should be addressed to:

RAL Library
STFC Rutherford Appleton Laboratory
Harwell Oxford
Didcot
OX11 0QX

Tel: +44(0)1235 445577
email: library@stfc.ac.uk

Science and Technology Facilities Council reports are available online at: https://epubs.stfc.ac.uk

Accessibility: a Microsoft Word version of this document (for use with assistive technology) may be available on request.

DOI: 10.5286/stfctr.2026018

ISSN 2753-5797

Variations in ISIS target plate thermal conductivity from mining ISIS machine databases

D J S Findlay, M Romanovschi, G D Howells, D Wilcox, S D Gallimore
ISIS Spallation Neutron Source, Rutherford Appleton Laboratory

August 2026

Abstract

Decreases in thermal conductivity of tungsten in the neutron-producing target in the ISIS First Target Station due to proton-beam-induced radiation damage have been measured by analysing data in automatically recorded databases of ISIS machine parameters. The analysis is based on measurements of target plate temperature decay rates when the proton beam irradiating the target is suddenly switched off. Results presented in this report extend the range of the first measurements of tungsten thermal conductivity made on an operational spallation neutron target published previously.

1. Context

In a recent publication [1], measurements of temperature decays in the new-style tantalum-clad ten-plate tungsten target for the ISIS First Target Station (TS-1) [2] were analysed to provide information on changes in tungsten thermal conductivity k as proton-beam-induced damage to the tungsten in the target increases — the first such measurements to have been obtained directly from an operating spallation neutron target. The analysis was based on high-time-resolution measurements of target plate temperature decay rates when the proton beam irradiating the target was suddenly switched off, since the rate at which temperatures decrease in a surface-cooled target plate when internal heat generation suddenly goes to zero depends on the thermal diffusivity $\alpha = k/(\rho c)$ within the plate (ρ and c being respectively density and specific heat), and so, other things being equal, a decrease in thermal conductivity k is accompanied by a slower rate of decay of the plate temperature.

However, in [1], the plate temperature decays selected for analysis had to be found by tedious visual inspection of proton beam current and target plate temperature databases, and inevitably this limited the number of such decays that were analysed[1]. The present report describes results of automatically scanning data held in ISIS machine databases, automatically identifying proton beam on-to-off transitions, and automatically measuring temperature decay rates, and so the number of target plate temperature decays that can be analysed has been greatly increased.

In the interests of readers' convenience, the present report includes some material already published in [1].

[1] For each of plates 2–9 inclusive, thirty-six temperature decays spanning February 2023 to March 2025 were analysed.

2. Spallation targets and thermal conductivity

Targets for the production of neutrons by proton-induced spallation have to be carefully designed for optimum performance, as requirements for high neutron output always have to be balanced against requirements for the provision of suitable cooling [3]. For solid spallation targets, tungsten is a good choice of target material, as it represents a good combination of high atomic number (to maximise neutron production) and good thermal conductivity (to facilitate cooling). But spallation targets must also be designed for long life, and existing measurements [4–11] show that the thermal conductivity of tungsten decreases as material damage (displacements per atom[2] (DPAs)) in the target plate material increases. Therefore designs of tungsten spallation targets must take into account this decrease in thermal conductivity as time goes on and irradiation of the target progresses.

Previous measurements of changes in tungsten thermal conductivity [4–11] have been made using laser-based methods on specially prepared tungsten samples after irradiation of the samples by spallation neutrons, by reactor neutrons, and by ions. Reductions in tungsten thermal conductivity of up to ~50% were found by the time irradiation had reached ~10 DPAs. However, these measurements were made on relatively small individual samples, whereas, at least in the case of the target in the First Target Station at the ISIS Spallation Neutron Source [2], the tungsten is in the form of a very much larger composite water-cooled assembly, the tungsten plates are clad in tantalum (a cladding process that involves hot isostatic pressing (HIP)), the proton beam is pulsed with a very small duty factor (proton beam current pulses ~0.5 μs long at a rate of 40 pulses per second), and the irradiating fluxes are far from being uniformly distributed throughout the target. It has seemed worthwhile, therefore, to take advantage of the possibility of 'mining' ISIS machine databases to make thermal conductivity measurements on a proton-driven spallation neutron target whilst it was actually operating, in order to uncover any differences that there might be between thermal conductivity behaviour in small uniform samples and in large manufactured non-homogenous assemblies — differences that could well be expected to be of interest to designers and operators of spallation neutron facilities.

3. ISIS TS-1 target

The measurements set out in the present paper were made on the ISIS new-style TS-1 ten-plate tantalum-clad tungsten target, a schematic diagram of which is shown in Fig. 1. The ten-plate 5.3-cm-radius target core is made up of a sequence of tungsten discs/cylinders clad in 1.5 mm of tantalum. Thicknesses of plates 1–10, including 1.5 mm tantalum cladding on both front and back surfaces, are respectively 14, 15, 17, 19, 19, 22, 26, 32, 40 and 146 mm, and the cooling channels between the plates are 2 mm wide. The target core is enclosed in a stainless-steel pressure vessel, and heavy water (D_2O) coolant is pumped through the target and is split essentially equally amongst the ten cooling channels leading to flow speeds of ~5.7 m s^{-1} over the plate surfaces and to normal target plate operating temperatures ranging from ~200°C at the front of the target down to ~50°C at the back. A 2-mm-diameter insulated-junction type-K thermocouple penetrates to the centre of each plate in order to measure the temperature of the plate. The 800-MeV proton beam spot on the front of the target has

[2] Hereinafter, except where explicitly stated otherwise, DPAs are NRT (Norgett, Robinson and Torrens) DPAs [M J Norgett, M T Robinson and I M Torrens, Nucl. Eng. Design 33 (1975) 50].

a nominal mean radius of 3.19 cm (see Sect. 5.6), and the work described in the present paper covered integrated beam currents up to 1320 milliamp-hours at proton beam currents of ~130–160 μA implying proton current densities of ~4.5 μA cm^{-2}. Throughout the time spanned by the measurements analysed in the present report, 'pumps-on' coolant flow rates were always within the range 480–485 litres minute^{-1}.

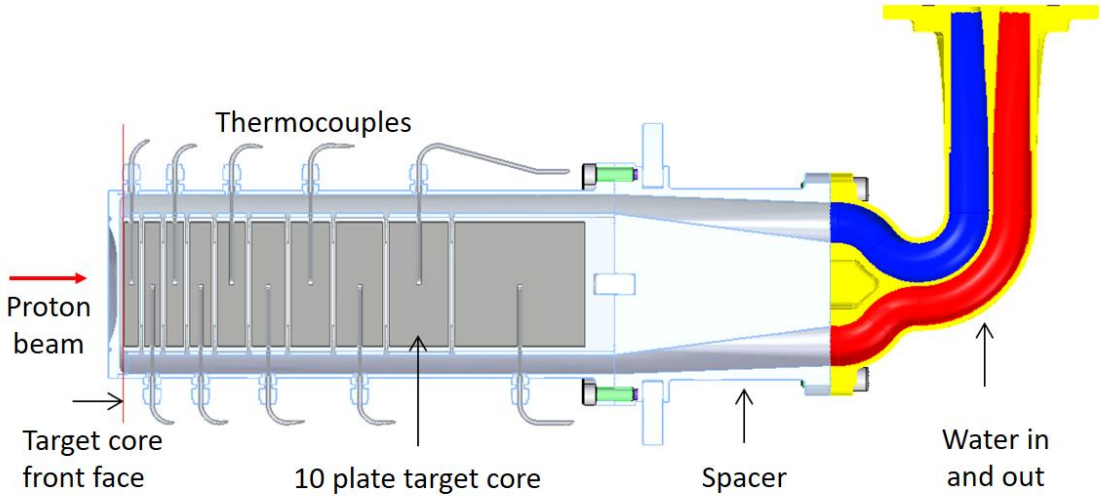

Fig. 1. New-style ISIS TS-1 neutron-producing target, horizontal section. The 10-plate target core (plate 1 at left-hand side, plate 10 at right-hand side) is essentially made up of a sequence of tungsten discs/cylinders clad in 1.5 mm of tantalum. The tantalum cladding is bonded to the tungsten discs/cylinders by hot isostatic pressing (HIP), and the resultant plates are electron-beam welded together to form the 5.3-cm-radius 10-plate target core. The D_2O water channels between the plates are 2 mm wide. The target core is surrounded by a stainless-steel pressure vessel the front of which serves as the window through which the irradiating proton beam passes and which is shaped to form the input and output cooling water manifolds.

4. Data

The ISIS machine databases that were made use of in the present work are those that record the proton beam current to the ten-plate TS-1 target and record the temperatures of the TS-1 target plate numbers 2–9 inclusive. (Thermocouple readings from plate 1 have been anomalous ever since the target was installed [12], and so plate 1 is excluded from the present analyses. Also excluded from the present analyses is plate 10, which acts essentially as a beam stop [13] and has too low a beam-on temperature and too slow a response when the beam is suddenly switched off to be useful.) Data from these databases were converted into CSV (comma-separated values) files, each file covering one 24-hour day. Examples of these CSV files are given in Table 1. Total disc space occupied by the CSV files covering beam current and target plates 2–9 between January 2023 and March 2026 inclusive was 47 gigabytes.

```
timestamp,LOCAL::BEAM:TARGET
2025-12-18 00:00:00.354494333,153.58281
2025-12-18 00:00:02.911446332,153.17343
2025-12-18 00:00:04.210430383,153.15077
2025-12-18 00:00:05.522412300,153.075
2025-12-18 00:00:06.770382404,153.11327
2025-12-18 00:00:08.012366294,153.31796
2025-12-18 00:00:09.270350456,153.4203
2025-12-18 00:00:10.523334026,153.03593
2025-12-18 00:00:11.790302515,153.27657
2025-12-18 00:00:13.068286418,153.25078
2025-12-18 00:00:14.387270450,153.30469
2025-12-18 00:00:15.646243095,153.13046
2025-12-18 00:00:16.886222362,153.32578
2025-12-18 00:00:18.113206386,152.86015
2025-12-18 00:00:19.365190505,153.2664
2025-12-18 00:00:20.587170362,153.28516
2025-12-18 00:00:21.862142324,153.33984
2025-12-18 00:00:23.108126401,153.12187
2025-12-18 00:00:24.380110502,153.19922
2025-12-18 00:00:25.649085760,153.41484
2025-12-18 00:00:26.924062490,153.38203
2025-12-18 00:00:28.187046289,153.27734
2025-12-18 00:00:29.473030328,153.35156
2025-12-18 00:00:30.750998497,153.26485
2025-12-18 00:00:31.987982511,153.14062
2025-12-18 00:00:33.211966514,153.49532
2025-12-18 00:00:34.441950321,153.14375
2025-12-18 00:00:35.709922790,153.13359
2025-12-18 00:00:36.947902441,153.17265
2025-12-18 00:00:38.207886457,153.25313
2025-12-18 00:00:39.460870504,152.98515
```

```
timestamp,TGT1:WTR:TGTTHERMS:TC102:TEMPERATURE
2025-12-18 00:00:00.810307264,154.4600067138672
2025-12-18 00:00:01.795337677,154.60000610351562
2025-12-18 00:00:02.801884174,154.32000732421875
2025-12-18 00:00:03.776545286,154.74000549316406
2025-12-18 00:00:04.745260953,154.44000244140625
2025-12-18 00:00:05.754219532,154.39999389648438
2025-12-18 00:00:06.774419546,155.0800018310547
2025-12-18 00:00:07.746498584,154.5800018310547
2025-12-18 00:00:09.734855890,154.6199951171875
2025-12-18 00:00:10.719811677,154.3800048828125
2025-12-18 00:00:11.689311027,154.1199951171875
2025-12-18 00:00:12.686888217,154.4600067138672
2025-12-18 00:00:13.688361883,154.32000732421875
2025-12-18 00:00:14.690443038,154.44000244140625
2025-12-18 00:00:15.725549221,153.9600067138672
2025-12-18 00:00:21.352597475,154.4600067138672
2025-12-18 00:00:24.405588626,154.16000366210938
2025-12-18 00:00:25.415413141,153.82000732421875
2025-12-18 00:00:26.426394939,154.24000549316406
2025-12-18 00:00:27.417194604,154.67999267578125
2025-12-18 00:00:28.408797740,154.52000427246094
2025-12-18 00:00:30.451464653,154.75999450683594
2025-12-18 00:00:31.432438373,154.52000427246094
2025-12-18 00:00:32.427110433,154.6199951171875
2025-12-18 00:00:33.408920764,154.10000610351562
2025-12-18 00:00:34.387832403,154.1999969482422
2025-12-18 00:00:35.365535736,154.0800018310547
2025-12-18 00:00:36.360657691,154.83999633789062
2025-12-18 00:00:37.333850860,154.67999267578125
2025-12-18 00:00:38.384049654,154.5399932861328
2025-12-18 00:00:39.371237039,154.33999633789062
```

Table 1. First few lines of CSV files for beam current to TS-1 and temperature of plate 2 in TS-1 target for 18 December 2025.

Gaps of several seconds sometimes occur in the database files, and so analyses of beam current and target temperature data recorded in these files must take occurrences of such gaps into account. And, no doubt in order not to waste database storage space, once the beam current goes to zero, no further beam current values are recorded until the beam current rises again above zero.

Table 2 lists a typical frequency distribution of the intervals between successive time data points for the target plate temperature data analysed in the present report. The table clearly illustrates the existence of gaps in the data.

Fig. 2 shows two typical examples of target plate temperature decay data, for plates 2 and 9, the thinnest and thickest of the eight target plates being considered in the present work. It is quite clear that the rate of temperature decay for plate 9 (the thickest) is less than the rate of temperature decay for plate 2 (the thinnest). From the slopes of the decay curves, it is evident that it is sufficient for fits of models to such temperature decay data to span time intervals between 10 seconds before beam-off time and 20 seconds after beam-off time.

Bin (s)	No. of intervals in bin	Separation of intervals Mean (s)	St. dev. (s)
0.0–0.2	127620	109.0	158.2
0.2–0.5	19305446	1.5	7.2
0.5–1.0	23860334	1.4	13.4
1–2	1862796	18.0	89.4
2–5	888574	37.9	61.0
5–10	799351	42.1	65.8
10–20	33600	812.5	2789.3
20–50	14872	1285.9	4377.3
50–100	870	2922.9	8783.9
100–200	130	2931.0	8305.6
200–500	173	2046.6	4835.4
500–1000	40	5168.1	5638.4
>1000	107		

Table 2. Frequency distribution of the intervals between successive time data points for target plate 2 temperature data analysed in the present report, and measures of the separation of successive intervals. Since, in general, the standard deviations of separations are considerably greater than the means, implying that the underlying distribution describing the separations of the intervals is not the exponential distribution, the suggestion is that the separations of intervals of similar lengths are not distributed randomly. Perhaps the non-randomness has something to do with the 'mechanics' of the algorithms involved in recording the temperature data.

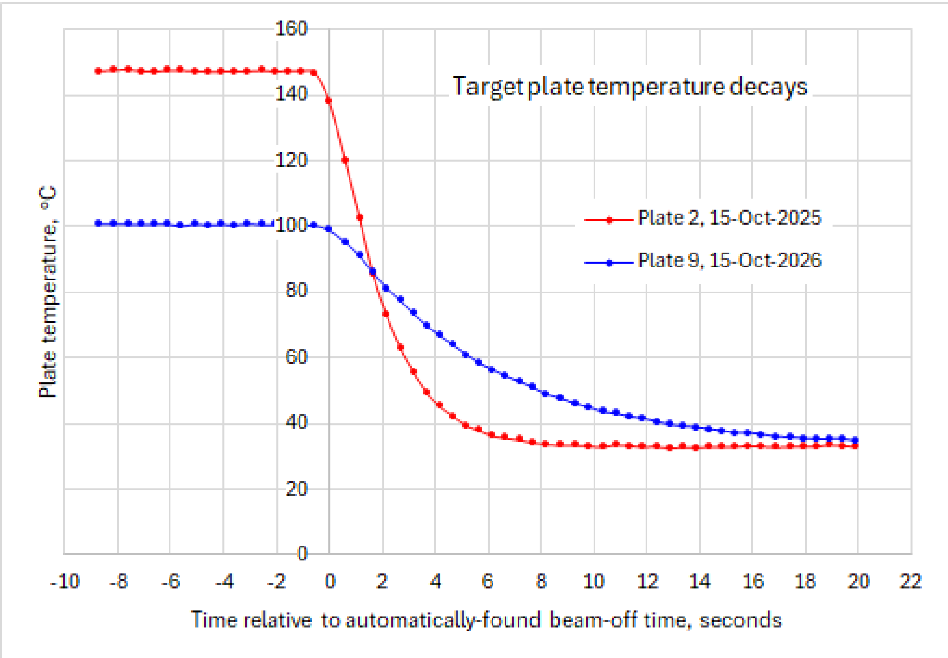

Fig. 2. Temperature decays in plates 2 and 9, the thinnest and thickest of the target plates being considered in the present work. The slower rate of decrease for the thicker target is clear.

5. Analysis

5.1 Method

In order to obtain values of thermal conductivity from decay rates of temperatures of target plates, a reliable method must already have been put in place for relating temperature decay rate to thermal conductivity, and for this purpose an existing ANSYS [14] model was used. The model, shown in Fig. 3, included 1.5 mm Ta cladding on all plates, a 0.25 mm water layer between core and vessel, and thermal conduction between adjacent plates. In order to establish interpolation grids for relating temperature decay rates to thermal conductivity, decay curves when the internal heat source within a plate is suddenly switched off were calculated for each plate for four values[3] of tungsten thermal conductivity k, *viz* 1.75, 1.46, 1.17 and 0.88 W cm^{-1} °C^{-1}.

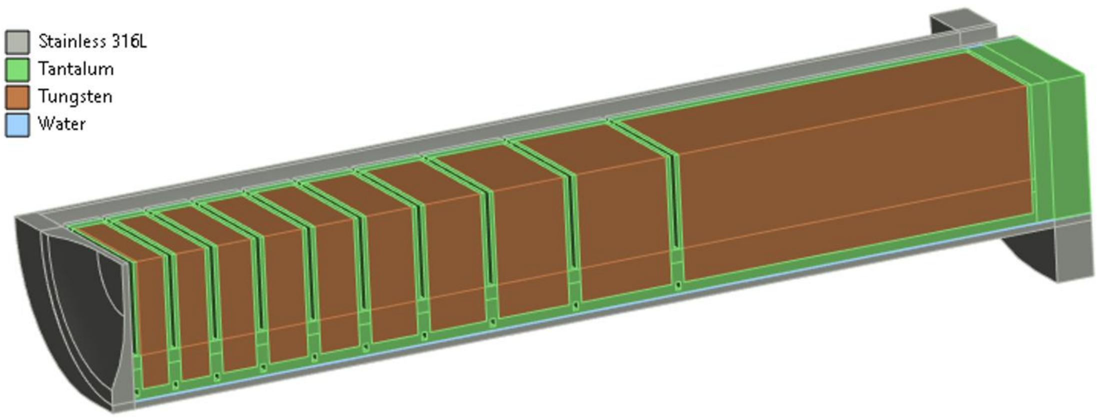

Fig. 3. One quarter of the ISIS new-style TS-1 target as modelled in ANSYS. In the modelling, the thermal conductivity of tungsten was assumed to be independent of temperature.

For each plate, since it was found that these calculated decay curves were not well fitted by single decaying exponential functions, sums of two decaying exponential functions $T = T(t) = U_1\exp(-t/\tau_1) + U_2\exp(-t/\tau_2) + U_{\text{cold}}$ were fitted to the calculated decaying temperatures curves in order to interpolate amongst the resultant four calculated decay curves, where U_1 and U_2 are the amplitudes of the decays and $U_{\text{cold}} = 35$°C is the coolant temperature assumed in the ANSYS calculations. These fits were carried out for target plates 2–9 and for the four values of k; fitted parameters are listed in Table 3, fits are shown in Fig. 4, and the results of the fits are shown in Fig. 5 wherein it is evident that $\tau_1 = \tau_1(k)$, $\tau_2 = \tau_2(k)$ and $(U_1/U_2) = (U_1/U_2)(k)$ are all well represented by power laws. Of course, there is an assumption here that ρ and c remain essentially constant, but there seems to be no good evidence to the contrary[4] [4].

[3] Thermal conductivity of tungsten at room temperature, and successive decreases of one sixth.
[4] In metals, radiation damage (point defects, dislocations, voids) has a minor direct effect on specific heat at high temperatures because the lattice heat capacity is dominated by phonons, which are not greatly altered by defect concentrations.

In view of the good representation of the three key parameters τ_1, τ_2 and U_1/U_2 of the ANSYS-calculated plate temperature decays by power laws in thermal conductivity k, measured temperature decays $T_{\text{data}} = T_{\text{data}}(t)$ when the beam to TS-1 was suddenly switched off should, at first sight, be fitted by the following function

$$T_{\text{fit}}(t) = T_{\text{hi}}, \qquad t \le t_{\text{off}}$$

$$T_{\text{fit}}(t) = U_1 \exp(-t/\tau_1) + U_2 \exp(-t/\tau_2) + T_{\text{lo}}, \qquad t > t_{\text{off}}$$

where $U_1 + U_2 + T_{\text{lo}} = T_{\text{hi}}$, $\tau_1 = a_1 k^{b_1}$, $\tau_2 = a_2 k^{b_2}$, $U_1/U_2 = a_3 k^{b_3}$, and t_{off} is the beam-off time. The four free parameters involved in the fitting would be T_{hi}, T_{lo}, t_{off} and k.

However, there is one more parameter that should be taken into account. Except for plate 10, which, as explained above, is not considered in the present work, the ANSYS calculations are calculations of the temperatures at the centres of target plates where the thermocouple tips within the target plates are nominally positioned, so that when internal heat generation is switched off there are discontinuous changes in slopes of the calculated temperatures as functions of time at the centres of the plates. But Fig. 2 shows quite clearly that there are not discontinuous changes in slope in the measured temperature curves when the beam is switched off; instead it is as if the 'true' measured temperatures as functions of time have been passed through a low-pass filter — presumably an effect of the finite response times of the thermocouples (response times of thermocouples are typically $\lesssim$1 second [15]). Consequently, the equation for $T_{\text{fit}}(t)$ set out above was passed through a digital low-pass filter before the resultant 'filtered' temperature function $T_{\text{fit}}^{\text{filtered}}(t)$ was fitted to the measured data, and the parameter characterising the filter cut-off frequency, τ_f in the present work, is the additional free parameter. Details of the low-pass filter, and justification of the values of τ_f used, are set out in Appendix 1.

In order to achieve reliable results, it is self-evident that the sudden beam switch-offs that are analysed must be 'good', *i.e.* before the beam is switched off the beam current should have been constant over a period of time $t_{I,\text{before}}$ sufficiently long to allow the target plate to have reached thermal equilibrium, and after switch-off the beam current I must remain at zero for time $t_{I,\text{after}}$ sufficiently long for the decay rate of the plate temperature to be able to be accurately determined. In the work described in the present report, $t_{I,\text{before}} = 20$ s and $t_{I,\text{after}} = 40$ s.

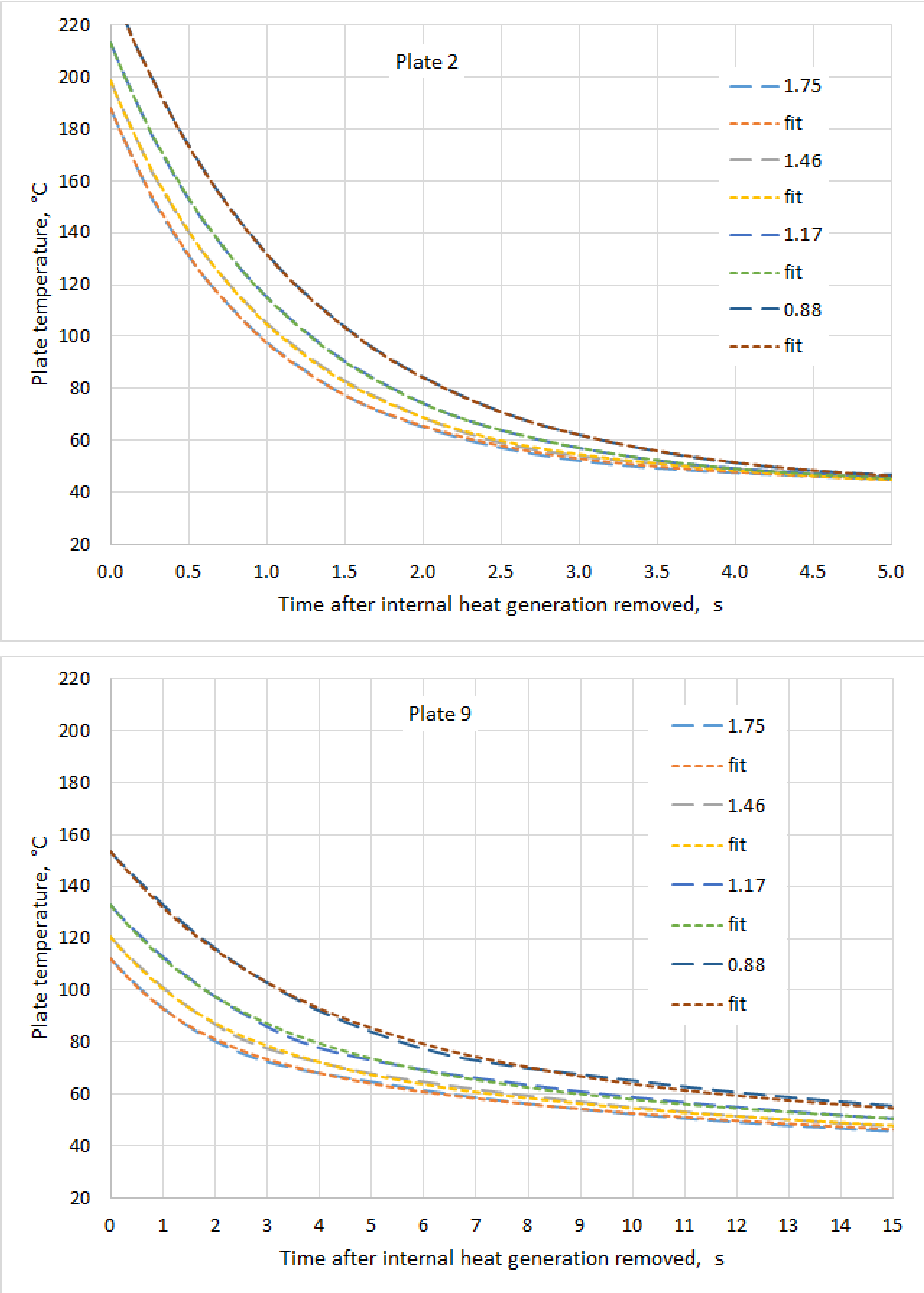

Fig. 4. Fits of $T(t) = U_1\exp(-t/\tau_1) + U_2\exp(-t/\tau_2) + U_{\text{cold}}$, sums of two decaying exponentials, to temperature dependences of target plate temperatures for k = 1.75, 1.46, 1.17 and 0.88 W cm^{-1} °C^{-1} calculated using ANSYS. See text for further details. (This figure has already been presented in [1].)

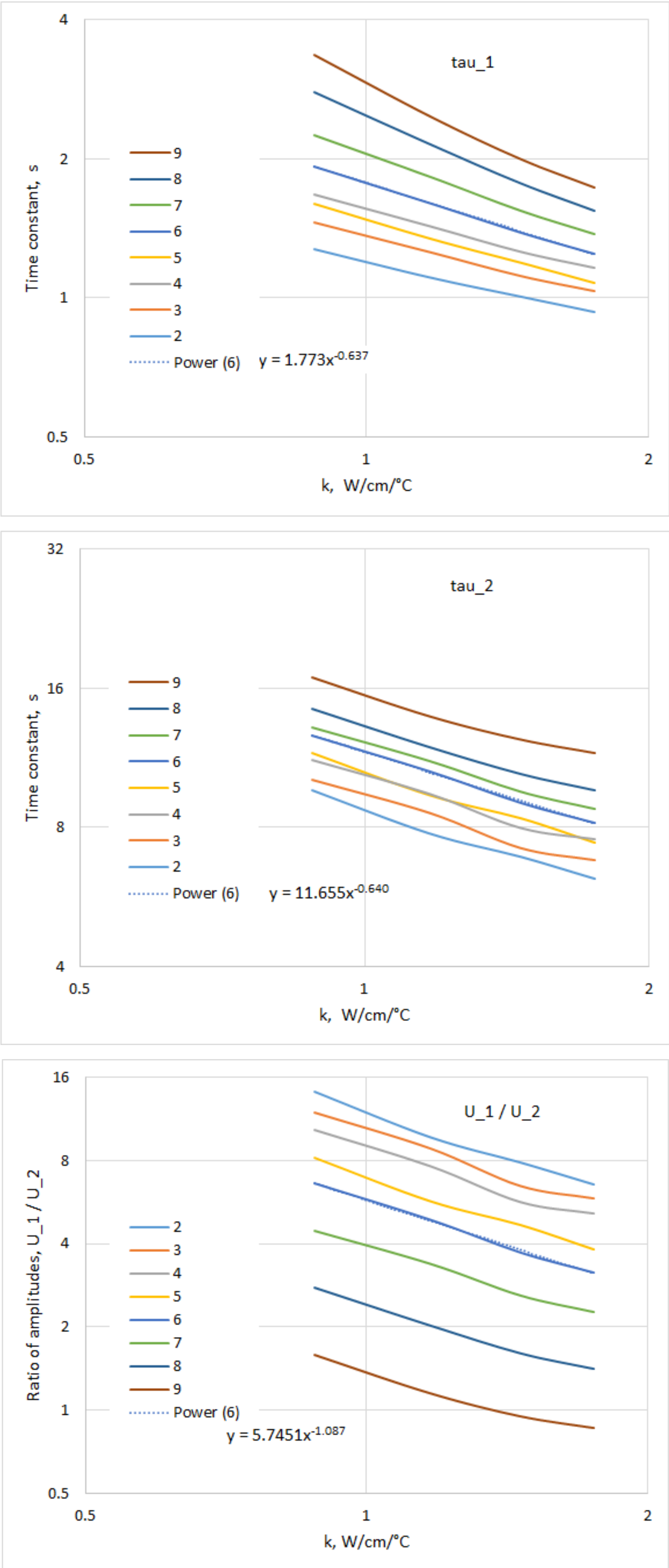

Fig. 5. Dependences of parameters τ_1, τ_2 and U_1/U_2 from fits to ANSYS calculations of target plate temperature decays as functions of thermal conductivity k as described in the text. Curve numbers correspond to plate numbers. 'Power' curves are power-law fits and parameters. (This figure has already been presented in [1].)

Plate	a_1	b_1	a_2	b_2	a_3	b_3	χ^2_{pdf}
2	1.1986	-0.4579	8.8428	-0.6652	12.1648	-1.1616	0.60
3	1.3612	-0.5042	9.4455	-0.6401	10.4215	-1.1316	0.92
4	1.5577	-0.5442	10.3961	-0.6188	9.0057	-1.0876	1.08
5	1.4849	-0.5780	10.6003	-0.6495	7.0204	-1.1134	1.38
6	1.7746	-0.6421	11.6819	-0.6498	5.7651	-1.1028	1.98
7	2.0493	-0.7351	12.1913	-0.6083	3.9427	-1.0352	1.78
8	2.4772	-0.8655	13.2503	-0.5934	2.4012	-1.0011	1.86
9	2.9206	-0.9771	15.3965	-0.5439	1.3665	-0.8909	1.59

Table 3. Parameters of power-law fits to ANSYS-calculated temperature decays as function of thermal conductivity k, $\tau_1 = a_1 k^{b_1}$, $\tau_2 = a_2 k^{b_2}$, $U_1/U_2 = a_3 k^{b_3}$. Values of the goodness-of-fit parameter $\chi^2_{\text{pdf}} = \sum_{i=1}^{N}\{(T_{\text{ANSYS},\,i} - T_{\text{fit},\,i})^2/(\delta T_{\text{ANSYS},\,i})^2\}/(N-n)$ ($n =$ number of free parameters) listed were obtained by assuming an ‘uncertainty’ of $\delta T_{\text{ANSYS},\,i} = 0.5$°C in all N temperature points i defining the calculated decay curves.

5.2 Identification of 'good' beam switch-offs

Identification of 'good' beam switch-offs for beam currents I between I_{lo} and I_{hi} was carried out by computerised scanning through successive 1-day CSV beam current files to find prospective switch-offs as follows:

- search through file to find instances where $I_{\mathrm{lo}} - \delta_I \le I(t_{i-1}) \le I_{\mathrm{hi}} + \delta_I$ and $I(t_i) \le \delta_0$ where the t_i's are the time values for successive lines in the files;
- read current values over period $t_{i-1} - t_{I,\,\mathrm{before}} \le t \le t_{i-1}$ and find minimum I_{min} and maximum I_{max} values of I;
- if $I_{\mathrm{max}} - I_{\mathrm{min}} > 2\delta_I$ reject this prospective switch-off;
- read current values over period $t_i \le t \le t_i + t_{I,\,\mathrm{after}}$ and find maximum value i_{max};
- if $i_{\mathrm{max}} > \delta_0$ reject this prospective switch-off;
- if not rejected as above, accept this prospective switch-off at time $t_{I,0} = t_i$ as a 'good' switch-off characterised by beam current $\bar{I}$ where $\bar{I}$ is the average value of beam current values over period $t_{i-1} - t_{\mathrm{before}} \le t \le t_{i-1}$.

In the work described in the present report, $I_{\mathrm{lo}} = 125$ μA, $I_{\mathrm{hi}} = 165$ μA, $\delta_I = 1$ μA, $\delta_0 = 1$ μA, $t_{I,\,\mathrm{before}} = 20$ s and $t_{I,\,\mathrm{after}} = 40$ s, and, as a result, 1305 'good' beam switch-offs were identified in the beam current database between January 2023 and March 2026.

5.3 Identification of 'good' temperature decays

Of course, even if a 'good' beam switch-off has been identified, it does not necessarily follow that the corresponding target plate temperature decay data are suitable to be fitted. Identification of 'good' temperature decays was therefore carried out as follows:

- given that temperature data are to be fitted over the range of times $t_{I,0} - t^{\mathrm{fit}}_{I,\,\mathrm{before}} \le t \le t_{I,0} + t^{\mathrm{fit}}_{I,\,\mathrm{after}}$ where $t_{I,0}$ is the beam switch-off time:
- if the number of temperature data points between $t_{I,0} - t^{\mathrm{fit}}_{I,\,\mathrm{before}}$ and $t_{I,0}$ is less than n_{before}, or if the greatest spacing in terms of time between any two successive of points is greater than $\delta^t_{\mathrm{before}}$, or both, reject this prospective temperature decay;
- if the number of temperature data points between $t_{I,0}$ and $t_{I,0} + t^{\mathrm{fit}}_{I,\,\mathrm{after}}$ is less than n_{after}, or if the greatest spacing in terms of time between any two successive points is greater than $\delta^t_{\mathrm{after}}$, or both, reject this prospective temperature decay.

In the work described in the present report, $t^{\mathrm{fit}}_{I,\,\mathrm{before}} = 10$ s, $t^{\mathrm{fit}}_{I,\,\mathrm{after}} = 20$ s, $n_{\mathrm{before}} = 5$, $\delta^t_{\mathrm{before}} = 2.0$ s, $n_{\mathrm{after}} = 10$ and $\delta^t_{\mathrm{after}} = 1.5$ s, and, as a result, for target plates 2–9, 108–115 'good' temperature decays were identified.

Evidently, only some ~10% of 'good' beam current switch-offs are associated with 'good' temperature decays. But this is understandable, as the time span over which data are fitted is 30 seconds long, whereas it can be seen from Table 2 that gaps in the data more than 2 seconds long occur on average more often than once every 37.9 seconds.

5.4 Supplementary data

In the recent publication [1], it is evident that just after irradiation of the target begins thermal conductivities of the plates appear to decrease quite rapidly, and so it was desirable to include in the present work as many temperature decay measurements in this 'early irradiation régime' as is reasonably possible. But, as has been seen in Sect. 5.3, as many as ~90% of 'good' beam current switch-offs are found to correspond to target plate temperature decays in the January 2023 – March 2026 databases that are insufficiently well defined. However, target plate temperature data had been recorded in another database which had been assembled for a particular purpose but which is not amenable to automatic scanning, and this database contains temperature measurements in regular 0.25-second steps rather than in steps of irregular length. For the early irradiation régime just mentioned, the 0.25-seconds-steps database was searched manually (albeit tediously) for suitable temperature decays, and these data are included in the present work.

5.5 Fitting

The 'filtered' temperature function $T_{\text{fit}}^{\text{filtered}}(t)$ described above was fitted to the measured temperature data $T_i^{\text{data}} = T^{\text{data}}(t_i)$ by least squares, *i.e.* by minimising $\chi^2_{\text{pdf}} = \sum_{i=1}^{N}\{(T^{\text{data}}(t_i) - T_{\text{fit}}^{\text{filtered}}(t_i))^2/(\delta T_i^{\text{data}})^2\}/(N-n)$ where N is the number of data points being fitted and n is the number of free parameters. Uncertainties δT_i^{data} in measured temperatures were taken everywhere as ±0.3°C. Values of χ^2_{pdf} were typically < 5.

For the minimisation routine [16] used to minimise the χ^2_{pdf}'s, starting values for the parameters T_{hi} and t_{off} were taken automatically from the average plate temperature over time $t_{I,\text{before}}^{\text{fit}}$ (Sect. 5.3) before beam switch-off, and from the beam switch-off time as found from the procedure described in Sect. 5.2. Starting values for T_{lo}, k and τ_f were always taken as 30°C, 1 W cm^{-1} °C^{-1} and 1 s.

The uncertainties in the values of the fitted parameters were obtained by repeating the fitting process 100 times with all data points perturbed by amounts chosen from a gaussian random number generator and then evaluating the standard deviations of the resultant sets of 'perturbed' parameter values, for each data point the standard deviation characterising the gaussian random number generator having been taken as the uncertainty in the data point.

5.6. Results

Results of the five-parameter fits (T_{hi}, T_{lo}, t_{off}, k, τ_f) are shown in Fig. 6. For ease of comparability with data that may arise in the future from other spallation neutron sources, values of the thermal conductivity and the thermocouple time constant are shown as functions of integrated proton beam current density on axis on the front face of the target, where, for the composite parabola-gaussian and two-parabola beam profile distributions that best fit measured profile data on the ISIS TS-1 target [17], integrated beam current density per square centimetre on axis q is 0.0313 × integrated beam current Q, implying a beam spot mean radius of 3.19 cm. Statistical uncertainties on the data points are nearly always smaller than the sizes of the plotted symbols.

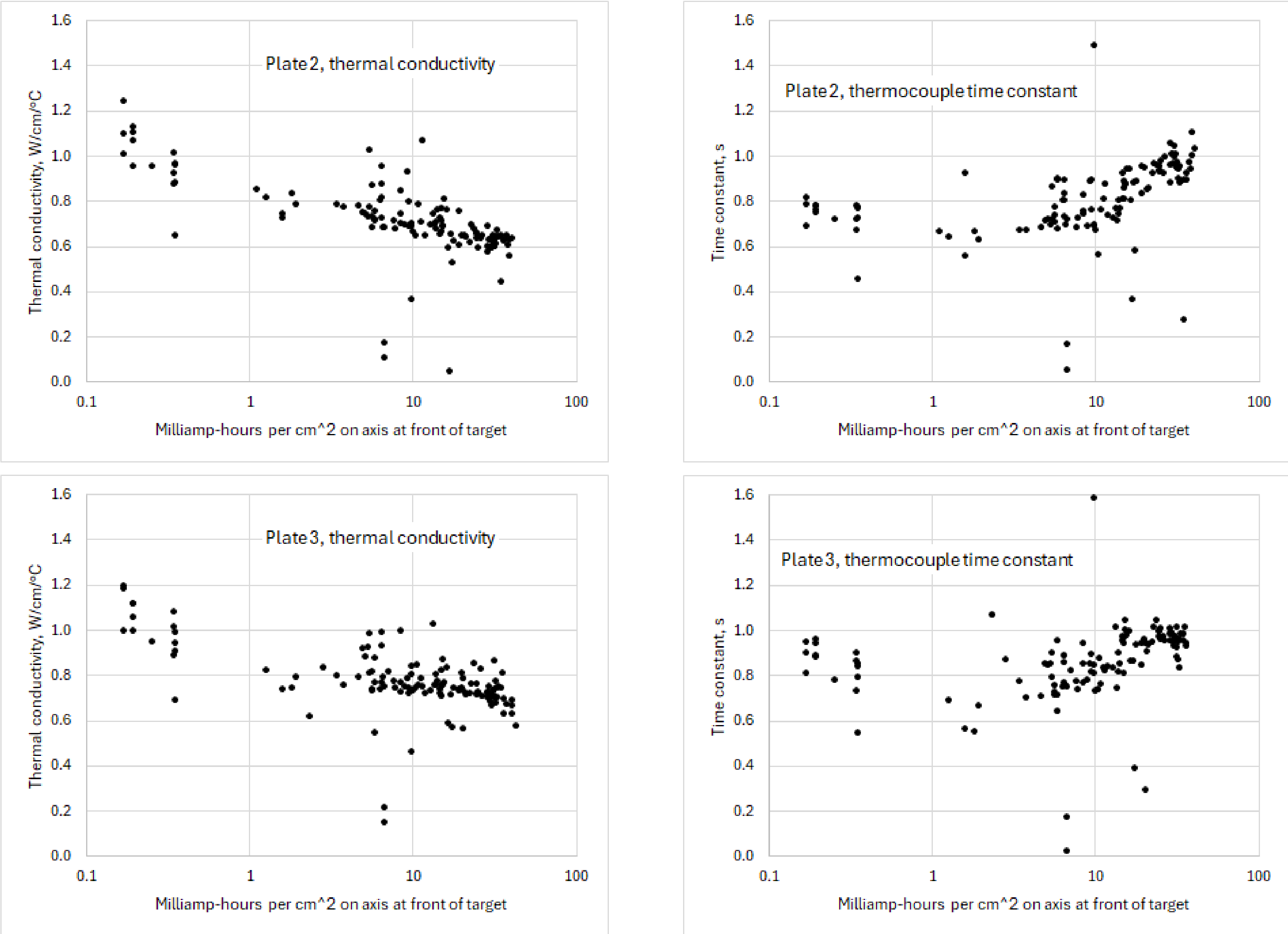

Fig. 6 (first part of four). Results of five-parameter fits to measured TS-1 target plate temperature decay data.

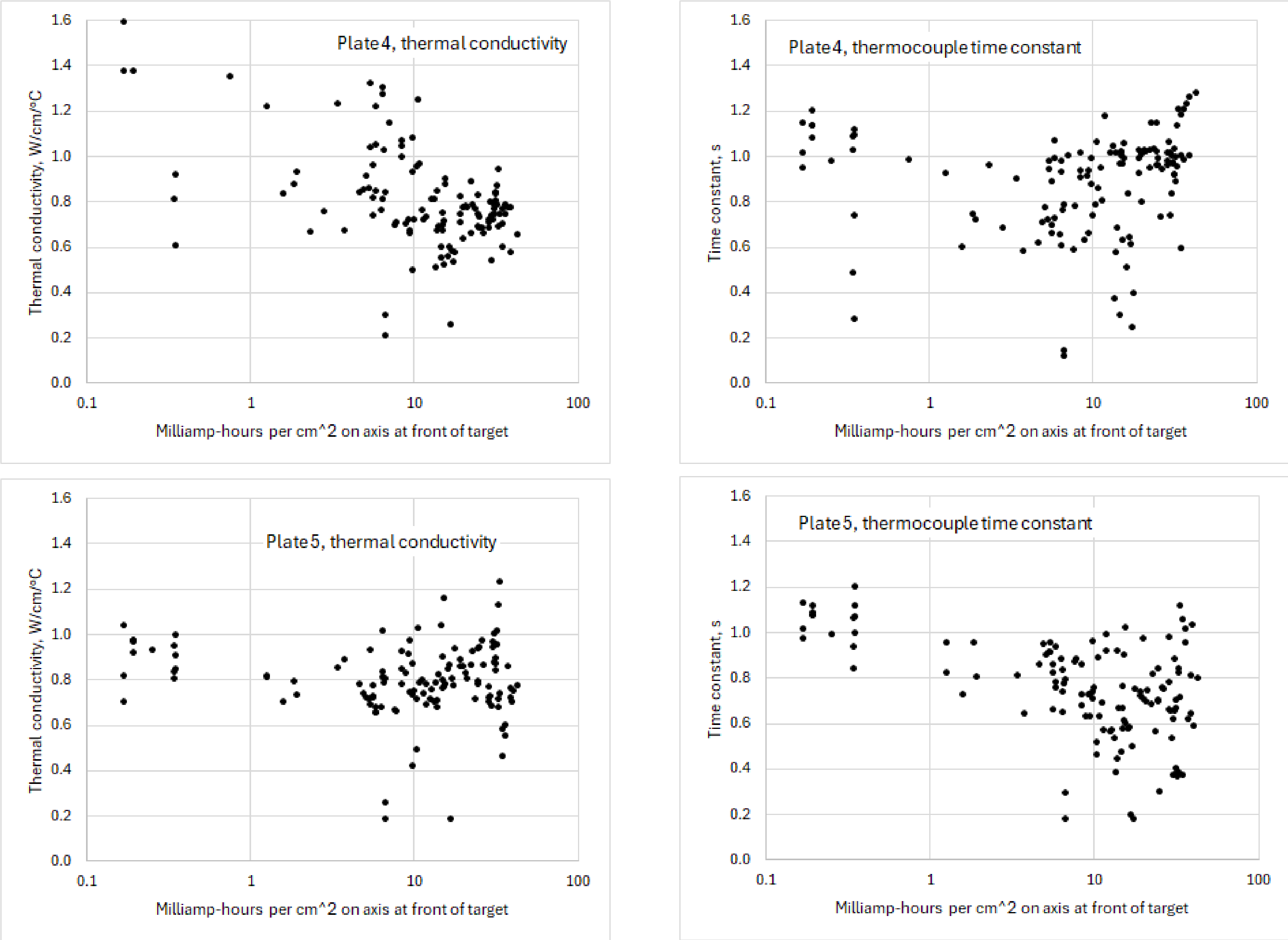

Fig. 6 (second part of four). Results of five-parameter fits to measured TS-1 target plate temperature decay data.

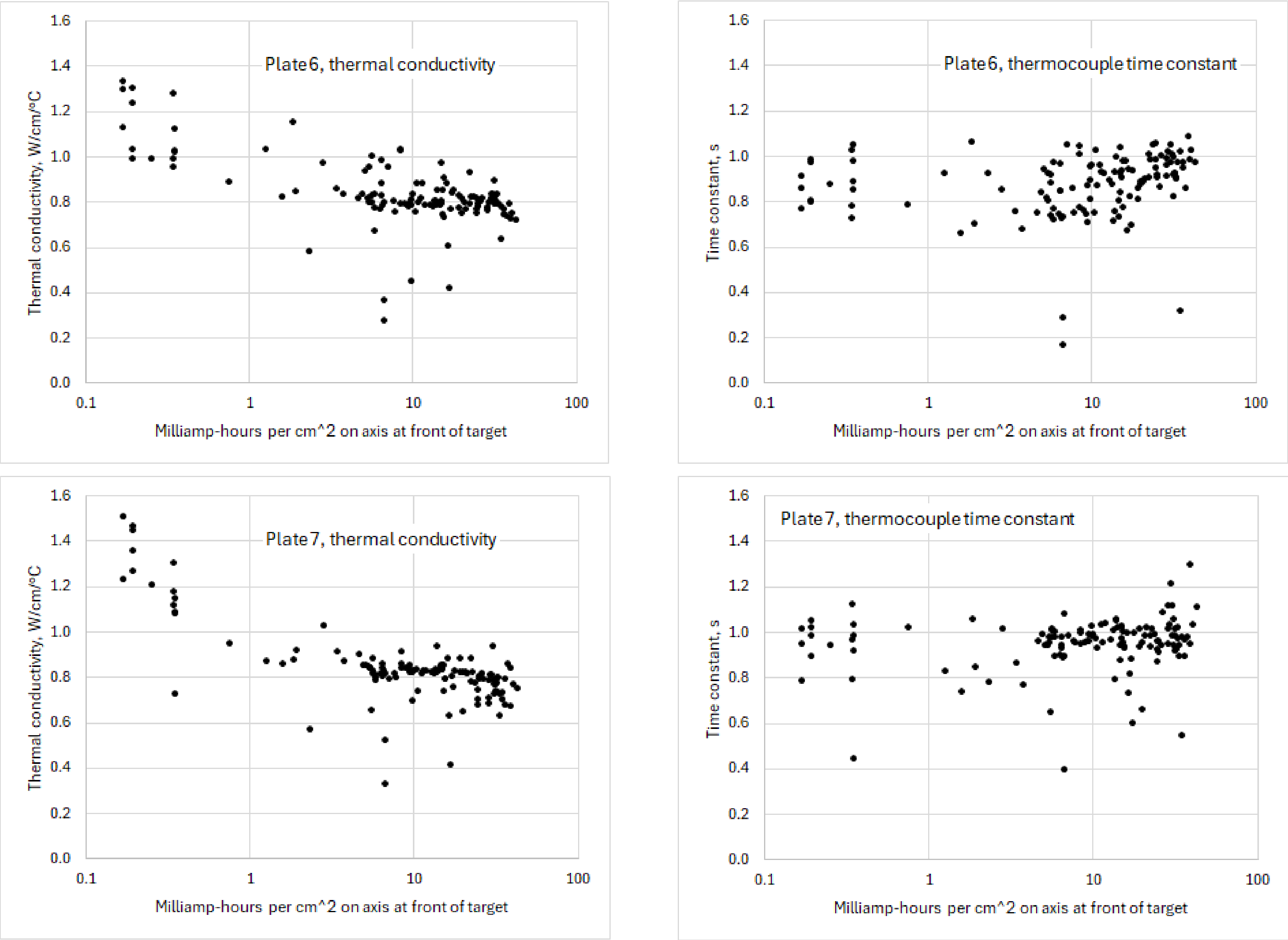

Fig. 6 (third part of four). Results of five-parameter fits to measured TS-1 target plate temperature decay data.

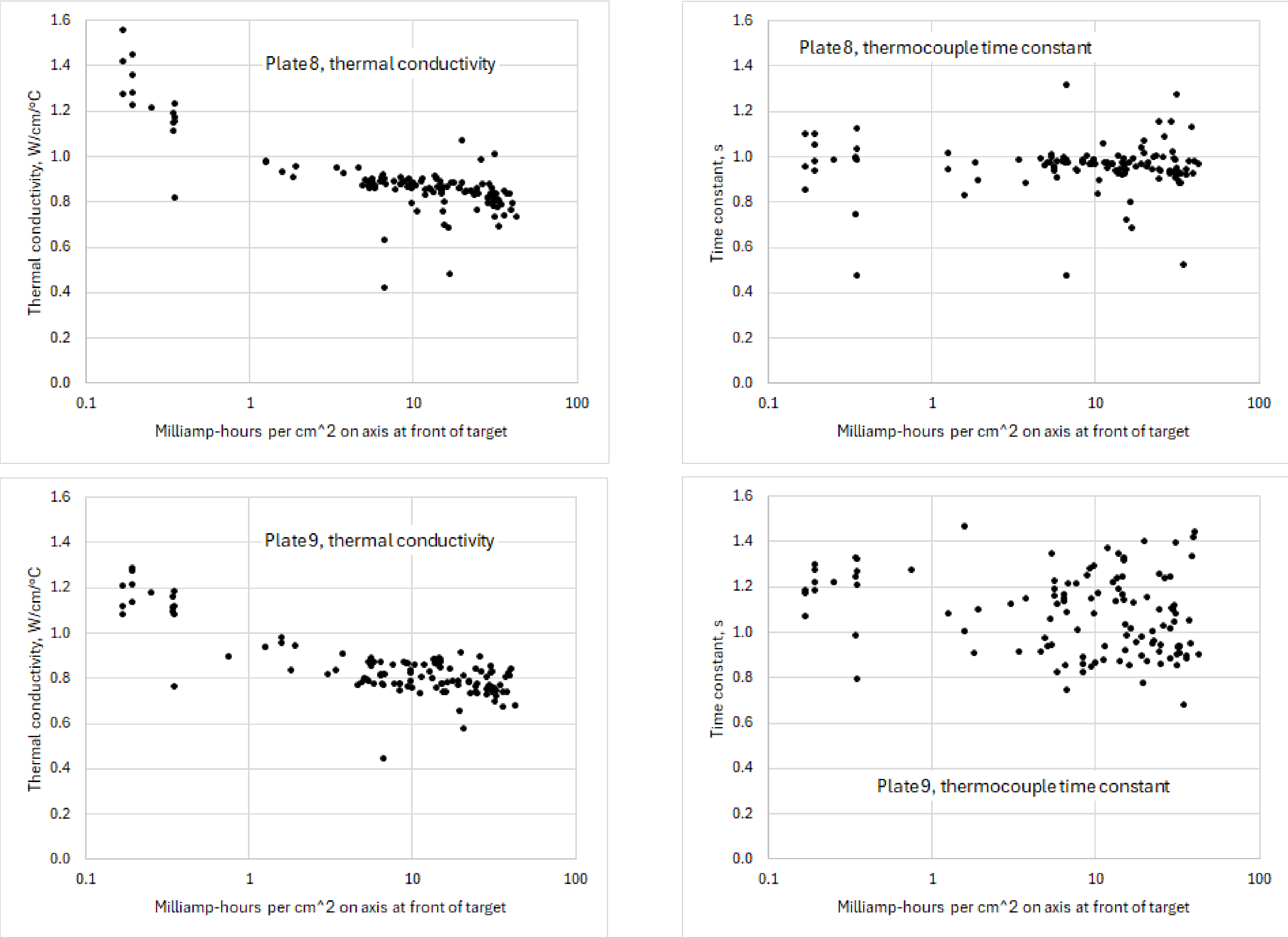

Fig. 6 (fourth part of four). Results of five-parameter fits to measured TS-1 target plate temperature decay data.

Taking the results shown in Fig. 6 at face value, it would appear that values of thermocouple time constants can vary as irradiation proceeds. Is it reasonable that the time constant of a thermocouple should vary with radiation damage within the thermocouple? An attempt at providing an answer is given in Appendix 1, wherein it is suggested that the time constant may increase by ~0.1–0.2 s if the effect of radiation damage is such as to halve the thermal conductivities of each of the three components of the thermocouple, *viz* wires, mineral insulation, and sheath.

If it be considered more plausible that for each plate the thermocouple time constant should always be the same, the thermocouple time constants for each plate can be averaged and then fixed at the average values during the fits to the measured temperature data. Averages and standard deviations of the thermocouple time constants are listed in Table 4.

Plate #	$\bar{\tau}_f$, s	σ_f, s
2	0.809	0.175
3	0.861	0.172
4	0.886	0.237
5	0.747	0.216
6	0.871	0.142.
7	0.950	0.137
8	0.959	0.127
9	1.090	0.207

Table 4. Averages $\bar{\tau}_f$ and standard deviations σ_f of values of thermocouple time constant τ_f when τ_f is regarded as a free parameter to be fitted to temperature data.

It is also evident in Fig. 6 that for each target plate the data points include some 'rogue' points. To investigate this further, frequency distributions of the corresponding χ^2_{pdf} values were assembled, and these are shown in Fig. 7. It is fairly clear from the plots that a plausible value of χ^2_{pdf} above which fits could be regarded as unsatisfactory is $\chi^2_{\text{pdf}} \approx 10$. Fig. 8 shows values of thermal conductivity k as a function of integrated beam charge per square centimetre delivered to target when the thermocouple time constants τ_f are fixed at the $\bar{\tau}_f$ values listed in Table 4, and when fitted values arising from fits with $\chi^2_{\text{pdf}} > 10$ have been discarded. Of course, it is recognised that there is always an element of subjectivity in identifying rogue data points, but some criterion has to be adopted, and the criterion being adopted here does not seem implausible. Table 5 lists the numbers of 'good' and discarded fits. Also shown in Fig. 8, for plates 2 and 9 (the thinnest and thickest plates being considered), are the sensitivities of k to τ_f.

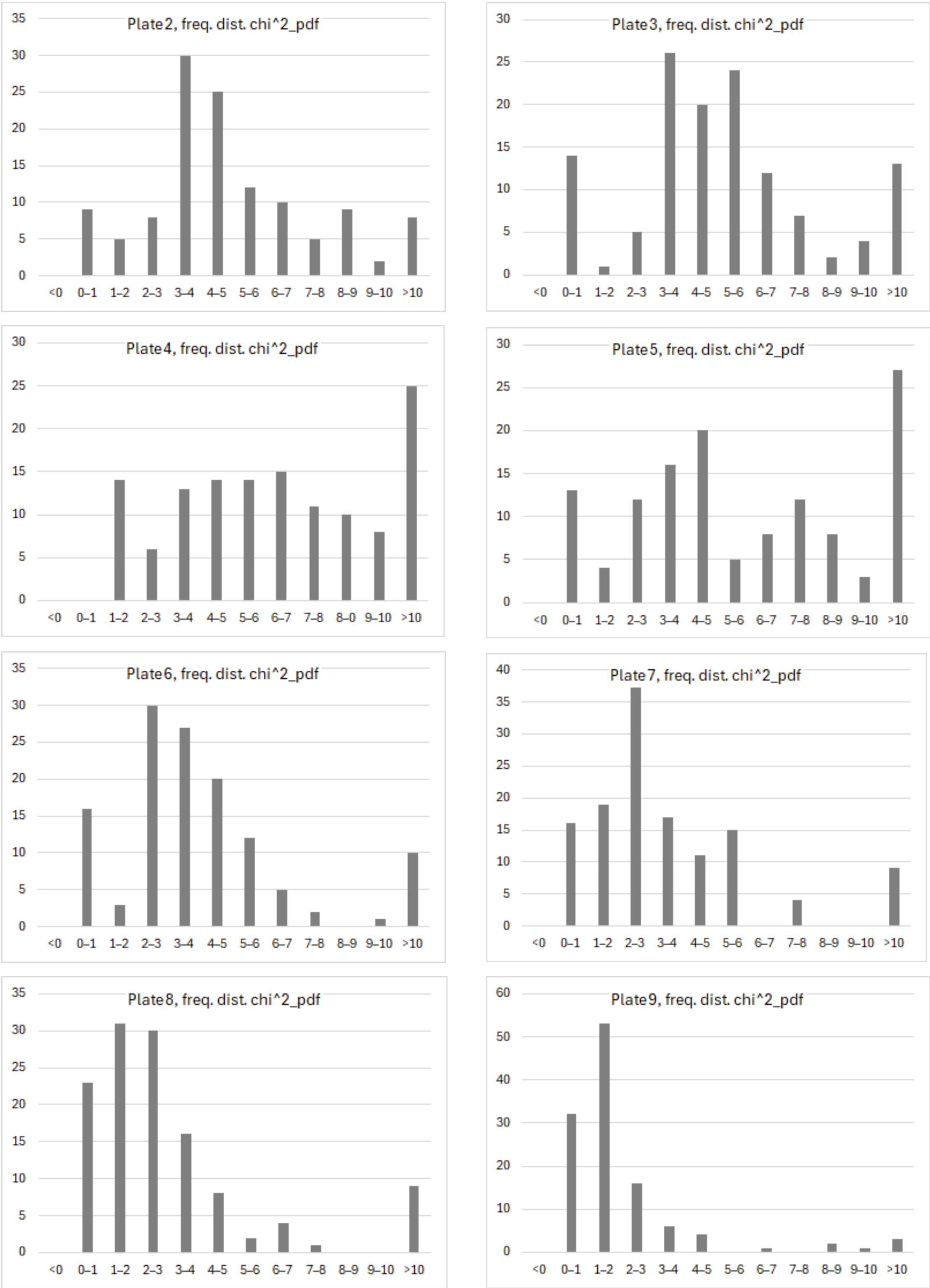

Fig. 7. Frequency distributions of χ^2_{pdf} values for the fits to measured temperature data for target plates 2–9 inclusive. These frequency distributions are for fixed-thermocouple-time-constant fits, but the distributions for free-thermocouple-time-constant fits are very similar.

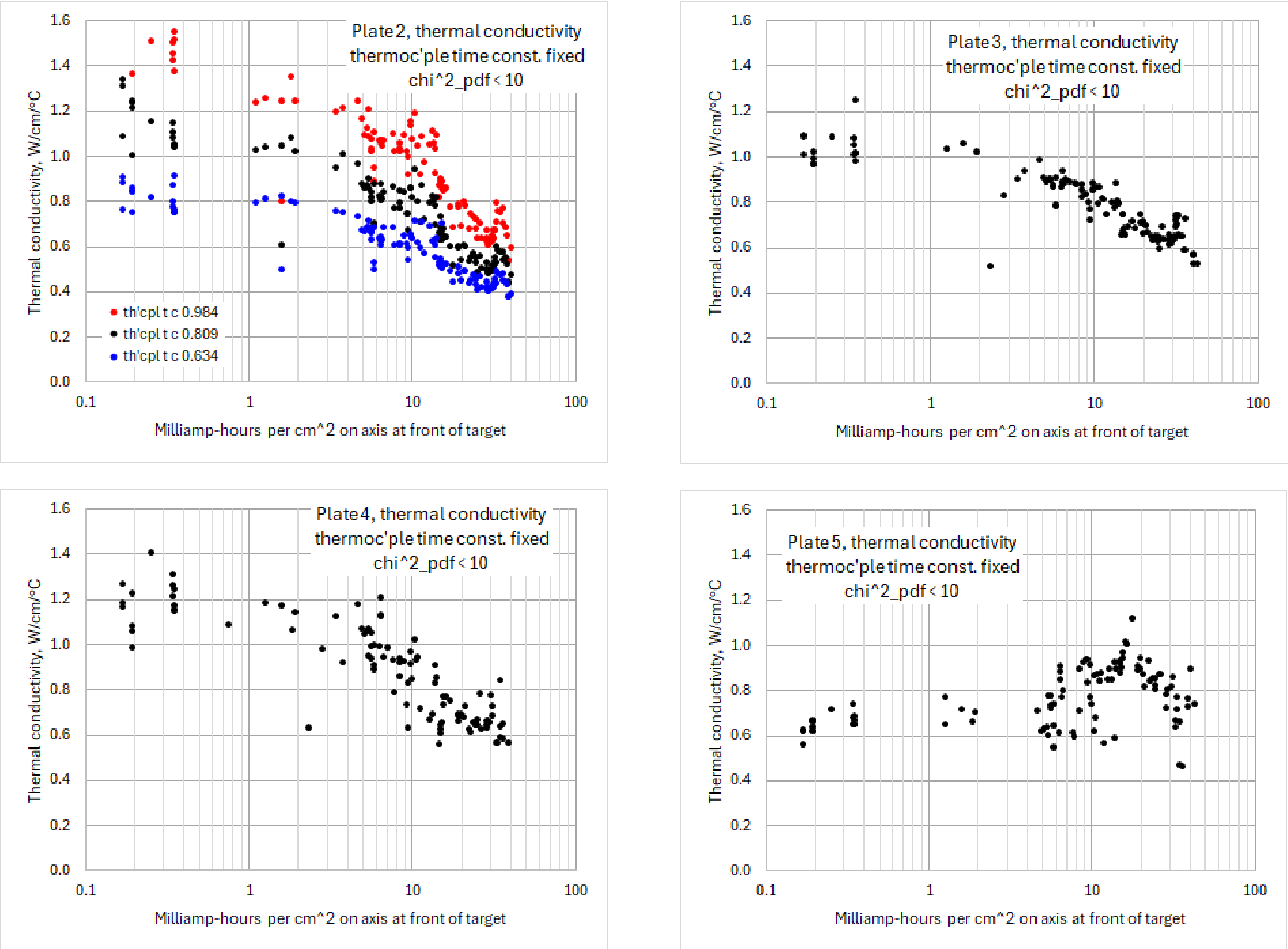

Fig. 8 (first part of two). Results of four-parameter fits to measured TS-1 target plate temperature decay data when rogue points have been discarded and the thermocouple time constants τ_f are fixed at the values listed in Table 4. For plate 2, sensitivities to τ_f are shown.

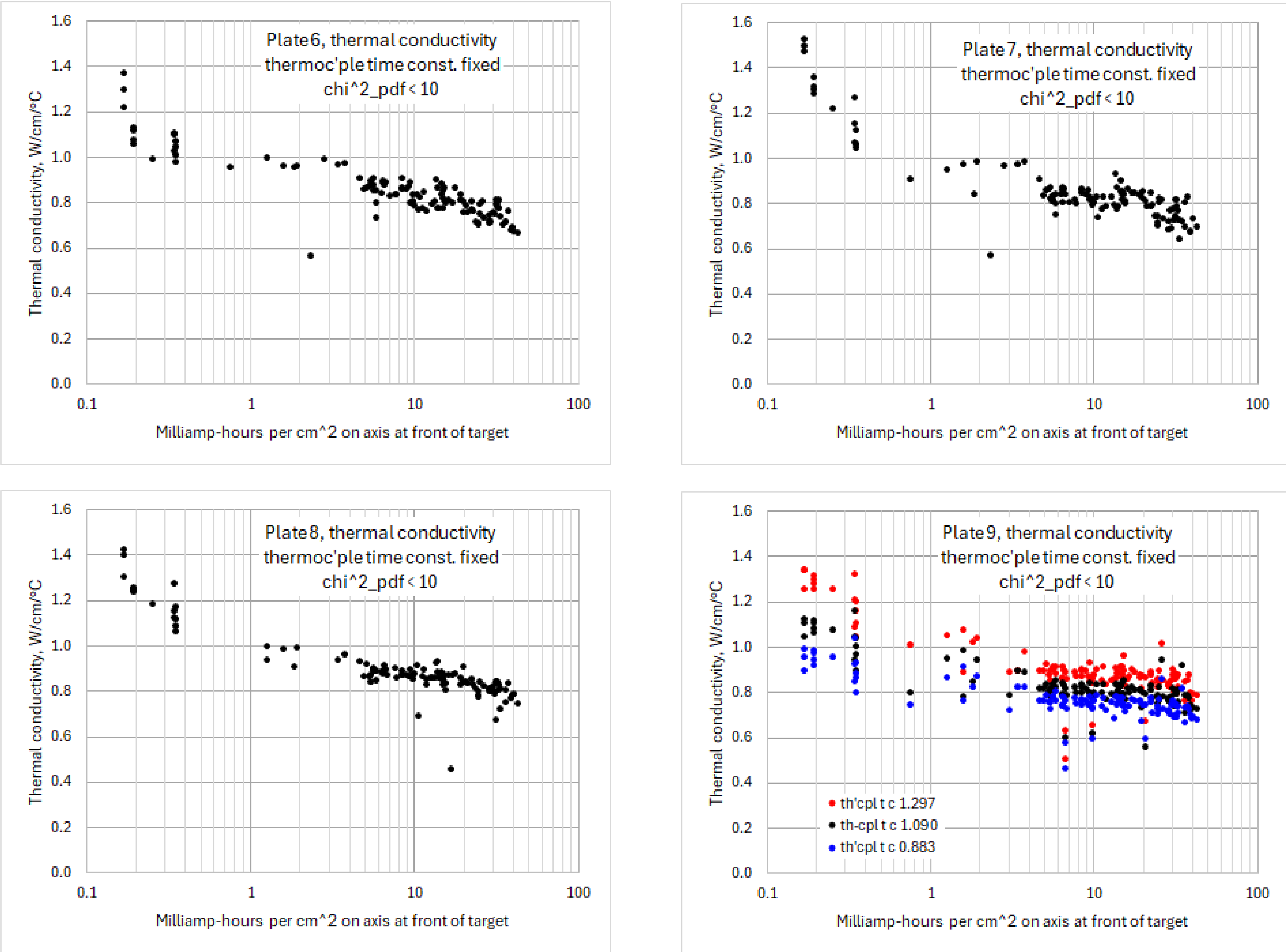

Fig. 8 (second part of two). Results of four-parameter fits to measured TS-1 target plate temperature decay data when rogue points have been discarded and the thermocouple time constants τ_f are fixed at the values listed in Table 4. For plate 9, sensitivities to τ_f are shown.

Plate	Total fits	Discarded fits
2	123	8
3	128	13
4	130	25
5	128	27
6	126	10
7	129	9
8	124	9
9	118	3

Table 5. Total numbers of fits to measured temperature decays, and numbers of fits discarded (as explained in the text) because the χ^2_{pdf}'s of the fits were too large.

5.7 Displacements per atoms (DPAs)

In material being irradiated, the number of displacements per atom N_{DPA} can be written as $N_{\mathrm{DPA}} = \int d\phi/dE(E)\ \sigma_{\mathrm{displ}}(E)\ dE$ where $d\phi/dE(E)$ is the fluence per unit energy of particles irradiating the material as a function of particle energy E, and $\sigma_{\mathrm{displ}}(E)$ is the atom-displacement cross-section for these particles. At the front of an ISIS target, where irradiating particles are protons all with the same energy E_0, $d\phi/dE(E) = \Phi\delta(E, E_0)$ where Φ is the fluence of the irradiating particles and δ is the delta function, whereupon $N_{\mathrm{DPA}} = \Phi\ \sigma_{\mathrm{displ}}(E_0)$.

From the ENDF/B NRT displacement cross-section for 800-MeV protons in tungsten of 8266 barns [18], and by converting mA-hours cm^{-2} (see Sect. 5.6) to numbers of protons cm^{-2}, 1 DPA becomes equivalent to 5.383 mA-hours cm^{-2} on axis at the front of the target where the 800 MeV proton flux dominates. Therefore, in Figs. 6 and 8, the range 0 – 43 mA-hours cm^{-2} corresponds to 0 – ~8 DPAs, and so the data in Figs. 6 and 8 can all be re-plotted in terms of DPAs at the front of the target.

In a similar way, from gas production cross-sections [19], at the front of an ISIS target the range 0 – 43 mA-hours cm^{-2} corresponds to 0 – ~4300 appm hydrogen production, and to 0 – ~750 appm helium production.

6. Discussion

As regards the results presented above, the two key points to be considered are probably the following:

1) irrespective of whether or not the thermocouple time constant τ_f is allowed to float free when fitting the measured temperature decay data, corresponding to the results in Figs. 6 and 8 respectively, it is evident that the values of tungsten thermal conductivity k in the target plates deduced from the analyses of the temperature data decrease as irradiation of the target increases; and
2) values of tungsten thermal conductivity k deduced from the analyses of the data increase as τ_f increases, and decrease as τ_f decreases.

The second of these points is not surprising. Essentially, the greater is the thermal conductivity of a plate, the faster is the rate of plate temperature decay when the irradiating proton beam is suddenly switched off, and so, when the smoothing effect of a constant thermocouple time constant is folded in, the greater proportionately is the change in the rate at which the thermocouple senses the decay of the plate temperature. Consequently, in Fig. 8, the 'vertical' difference between the red and blue points is greater for small values of integrated beam current density q than for large values of q (*i.e.* respectively the vertical differences at the 'left-' and 'right-hand' sides of the plots for plates 2 and 9), and the greater is the vertical distance between the red and blue points at small q for plates that decay at faster rates (*i.e.* the vertical distances at the left-hand sides of the plots for plates 2 and 9).

Given that it is most unlikely that the true values of the thermocouple time constants are likely ever to be measured, and given that if the time constants were found to vary their values would be likely to vary monotonically with q, probably, *faute de mieux*, the best interpretation for the results presented so far is to take the values of thermal conductivity shown in Fig. 8 as the black points but to assume uncertainties in the values varying systematically and gradually from ±30% at $q \approx 0.03$ mA-hours cm^{-2} to ±15% at $q \approx 30$ mA-hours cm^{-2}.

For four of the eight target plates 2–9, Fig. 9 shows comparisons of the values of tungsten thermal conductivity k from the present work with those of Habainy *et al.* [4], Peacock *et al.* [5] and Reza *et al.* [10] as a function of NRT displacements per atom (DPA) (where numbers of DPAs have been derived as in Sect. 5.7). (The values of thermal conductivity k attributed to Reza *et al.* have been derived from their measured values of thermal diffusivity $\alpha = k/(\rho c)$ assuming $\rho = 19.2$ g cm^{-3} and $c = 0.135$ J g^{-1}°C^{-1}.) It seems fairly certain that the present measurements of tungsten thermal conductivity are useful in filling in gaps between previously measured values.

As is evident in Figs. 6, 8 and 9, adjacent thermal conductivity data points often differ from each other by more than would be expected from the statistical uncertainties (which, as mentioned earlier, are generally smaller in size than the sizes of the plotted symbols). One reason for this may well be because there is no servo system in operation to hold constant the shape and size of the beam spot on the front face of the target; instead, the extent to which constancy is maintained depends on the vigilance of the accelerator physicists — and , of course, power deposition per unit area in a beam spot tends to vary as the square of the linear size of the beam spot.

Of the results in Fig. 8, those for plate 5 seem to be anomalous in that they hardly suggest a decrease in thermal conductivity with increasing beam deliver to target. However, the temperature readings from the thermocouple in plate 5 have been very noticeably noisy, as shown in Fig. 10, and so the results for plate 5 in the figures can probably be disregarded.

Is it possible that changes within target plates other than changes in thermal conductivity are mimicking the effects of changes in thermal conductivity? For example, could the tantalum cladding of a plate be gradually separating from the tungsten interior? Whilst a definitive answer cannot be given short of embarking on the operationally highly undesirable process of destructive examination of targets in a post-irradiation examination (PIE) cave, the likelihood is that cladding separation would occur suddenly and unpredictably depending on random manufacturing defects in particular plates, whereas what is observed, on average, for all plates, are gradually decreasing values of thermal conductivity as irradiation progresses.

Even though the sensitivity of the present values of thermal conductivity to thermocouple time constants may be something of an Achilles' heel, it is suggested that the significance of the present work is that the values of thermal conductivity have been obtained from a spallation neutron target as the target is actually being irradiated, in contrast to measurements made on small specially prepared samples. Further, in the present work, questions about effective irradiation temperatures and effective annealing temperatures within the target have effectively been by-passed.

7. Summary and conclusions

Values of thermal conductivity k of eight plates in the ten-plate spallation-neutron-producing target in the ISIS First Target Station (TS-1) have been measured as a function of radiation damage whilst the target is actually being irradiated. Approximately one hundred values of k have been obtained for each of the eight plates 2–9.

By the time the target has been irradiated to ~8 displacements per atom (NRT DPAs), the thermal conductivity of the tungsten has decreased from its 'book' value by ~50% — in essential agreement with measurements made previously by others on small specially prepared tungsten samples.

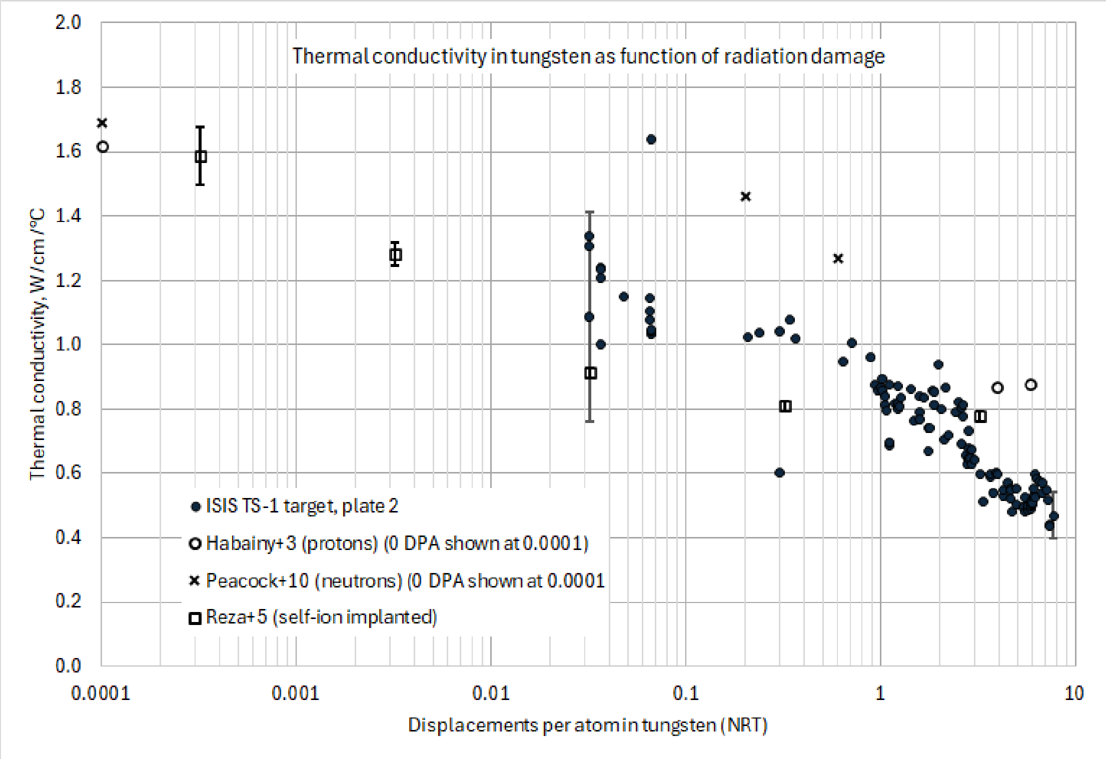

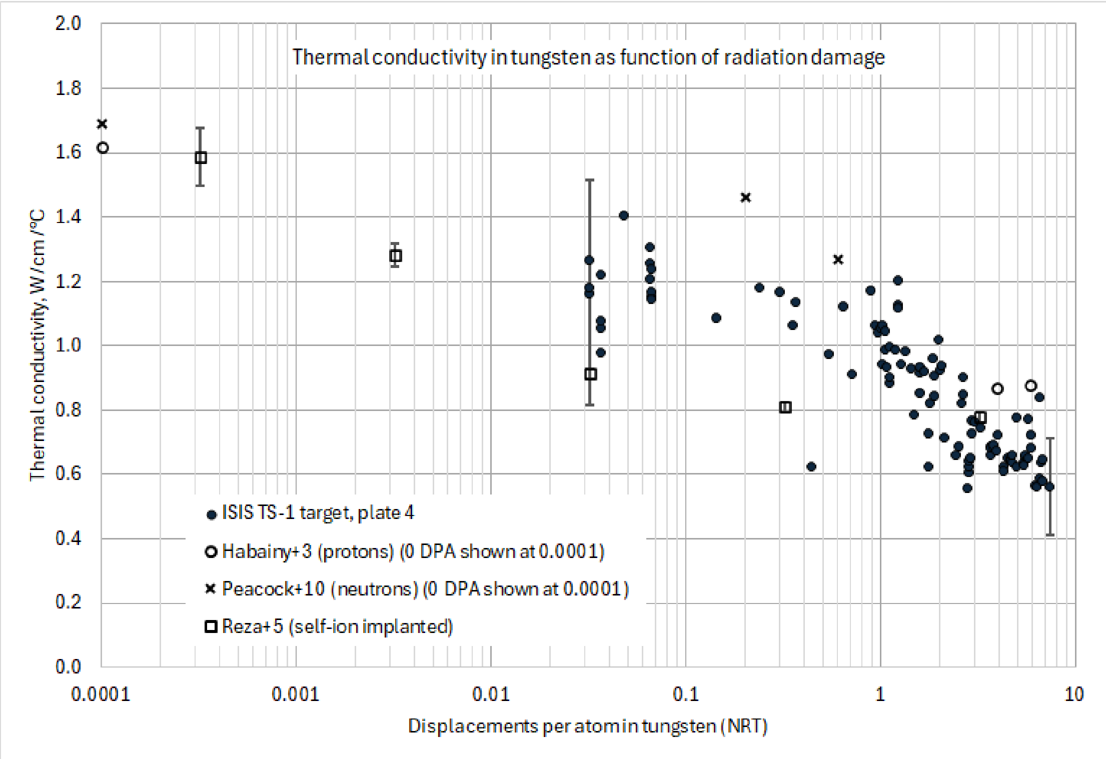

Fig. 9 (first of two parts). For target plates 2 and 4, comparison of the present values of tungsten thermal conductivity with those of Habainy *et al.* [4], Peacock *et al.* [5] and Reza *et al.* [10] as a function of displacements per atom (DPA, NRT) (Reza *et al.*'s thermal diffusivity results being converted to thermal conductivity as described in the text). (Because of the logarithmic scale, values for 0 DPA have been plotted at 0.0001 DPA). The error bars at the 'left-' and 'right-hand sides' of the present data are intended to show (as explained in the text) that the systematic uncertainty in the measurements varies gradually from ±30% at the left-hand side to ±15% at the right-hand side.

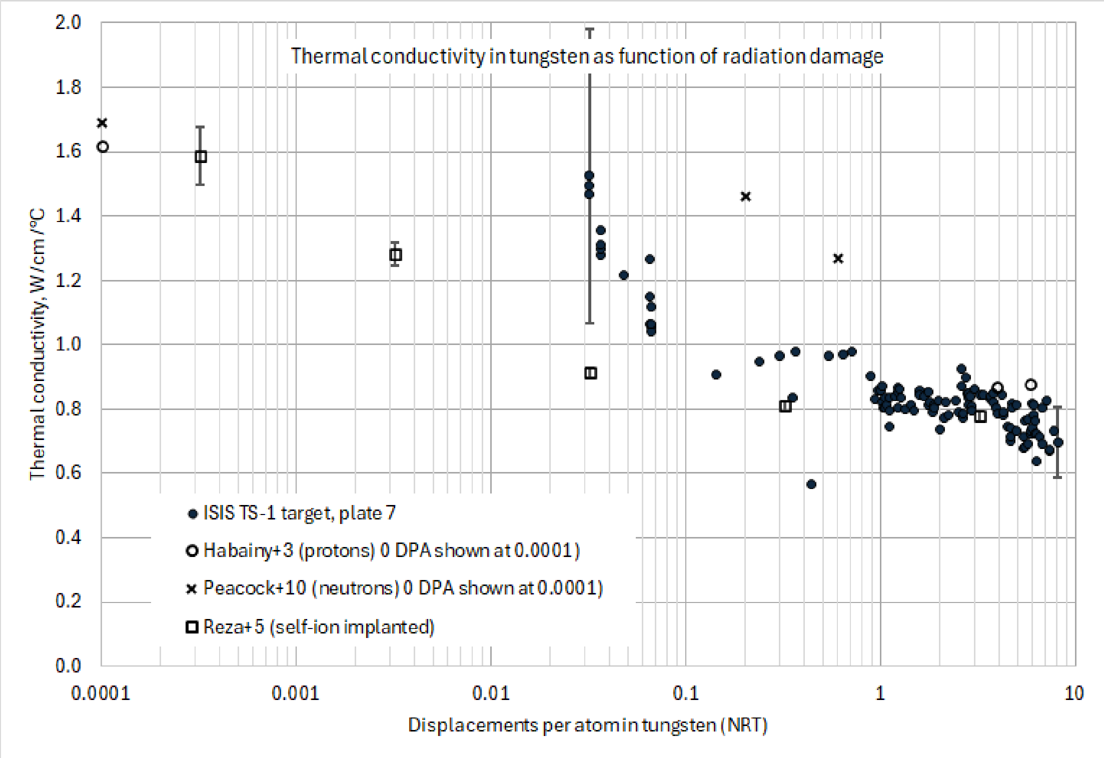

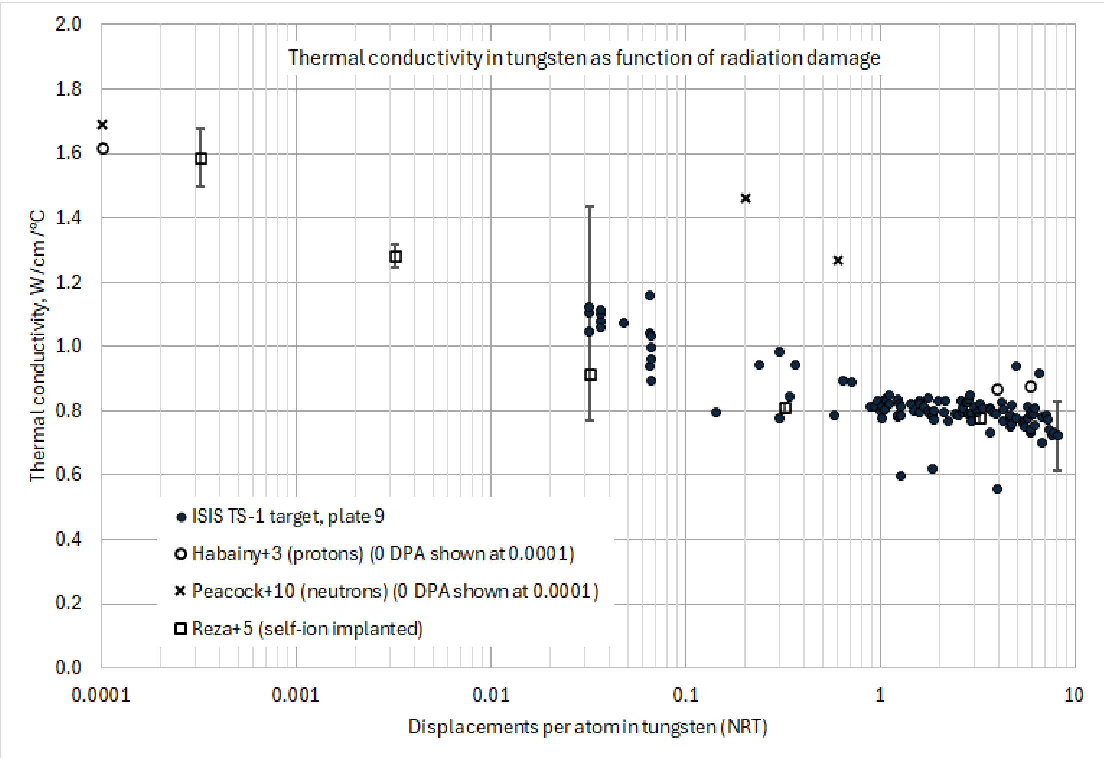

Fig. 9 (second of two parts). For target plates 7 and 9, comparison of the present values of tungsten thermal conductivity with those of Habainy *et al.* [4], Peacock *et al.* [5] and Reza *et al.* [10] as a function of displacements per atom (DPA, NRT) (Reza *et al.*'s thermal diffusivity results being converted to thermal conductivity as described in the text). (Because of the logarithmic scale, values for 0 DPA have been plotted at 0.0001 DPA). The error bars at the 'left-' and 'right-hand sides' of the present data are intended to show (as explained in the text) that the systematic uncertainty in the measurements varies gradually from ±30% at the left-hand side to ±15% at the right-hand side.

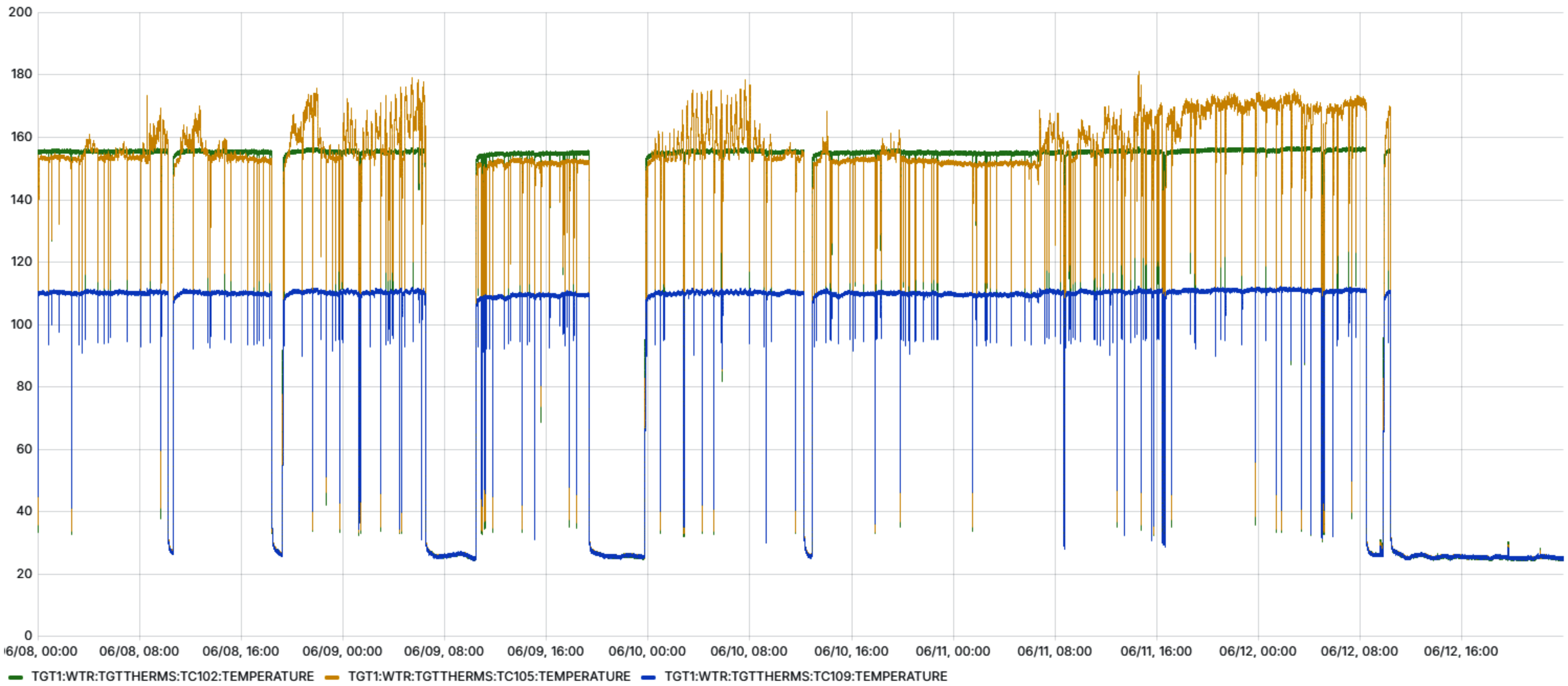

Fig. 10. Thermocouple temperatures readings from plates 2 (dark green), 5 (orange) and plate 9 (blue) during 8–12 June 2026. The noise on the (orange) signals from the thermocouple for plate 5 is very evident.

References

[1] D J S Findlay, D Wilcox, L Quintieri, G D Howells, D M Jenkins, J D Moor and S D Gallimore, Nucl. Instr. Meth. A 1089 (2026) 171555; https://doi.org/10.1016/j.nima.2026.171555.

[2] https://www.isis.stfc.ac.uk/.
Also J W G Thomason, Nucl. Instr. Meth. A 917 (2019) 61.

[3] For example, in: T A Broome, Proc. European Particle Accelerator Conf., 1996 paper TUY04A, https://accelconf.web.cern.ch/e96/papers/orals/tuy04a.pdf.

[4] J Habainy *et al.*, J. Nucl. Materials 509 (2018) 152.

[5] A T Peacock *et al.*, J. Nucl. Materials 329–333 (2004) 173–177.

[6] D R Mason *et al.*, Phys. Rev. Materials 5 (2021) 125407.

[7] H Sina *et al.*, J. Nucl. Materials 601 (2024) 155324.

[8] H Sina, ‘Thermal diffusivity of tungsten irradiated by protons in spallation environment up to 26.5 dpa’, HPTW 2023, RIKEN, Japan, November 2023.

[9] M Akiyoshi *et al.*, J. Nucl. Materials 543 (2021) 152594.

[10] A Reza *et al.*, Acta Materialia 232 (2022) 117926; https://doi.org/10.48550/arXiv.2111.07713.

[11] A P C Wylie *et al.*, J. Appl. Phys. 132 (2022) 045102.

[12] D J S Findlay *et al.*, Nucl. Instr. Meth. A 1059 (2024) 168986.

[13] D J S Findlay and L Quintieri, Nucl. Instr. Meth. A 1067 (2024) 169701.

[14] D Wilcox, ‘Transient Thermal Simulations of TS-1 Project Target after Irradiation’. internal RAL report, September 2025.

[15] For example, https://www.tcdirect.co.uk/thermocouple-sensors/thermocouple-response-times.aspx.

[16] VA24, Harwell Subroutine Library, https://www.hsl.rl.ac.uk/.

[17] D J S Findlay, B Jones and D J Adams, Nucl. Instr. Meth. A 889 (2018) 113.

[18] https://www-nds.iaea.org/public/download-endf/DXS/Displacement_XS/DXS.(2018)/Proton_irradiation/Files/ENDF_format/p_74_W0.dxs.

[19] https://www-nds.iaea.org/public/download-endf/DXS/Gas_Production_XS/DXS3000.(2011-2014)/Files/p_74_W.gxs.

[20] https://www.hsl.rl.ac.uk/.

[21] Tables of Physical and Chemical Constants, ed. Kaye & Laby, 15th edition, Longman, 1986.

[22] B Le Neindre *et al.*, J. Chem. Eng. Data, 21 (1976) 265.

[23] Report AECL-3689, Atomic Energy of Canada, 1971.

Appendix 1[5]. Response times of thermocouples in new-style TS-1 target

In the analysis described in the main text, allowance had to be made for finite ~1-second response times of the thermocouples embedded in the target plates, and so in this appendix are presented some simple calculations of what the response time of a target plate thermocouple might be. The essence of the matter could be summarised as follows: if an internally heated tantalum-clad target plate has reached thermal equilibrium, and if then the internal heat source is suddenly removed, what is the difference between the resultant decay curve for the temperature at the centre of the plate and the decay curve for the temperature as measured by the thermocouple embedded within the plate?

The internal construction of a plate in the new-style ISIS TS-1 target is outlined schematically in Fig. A1.

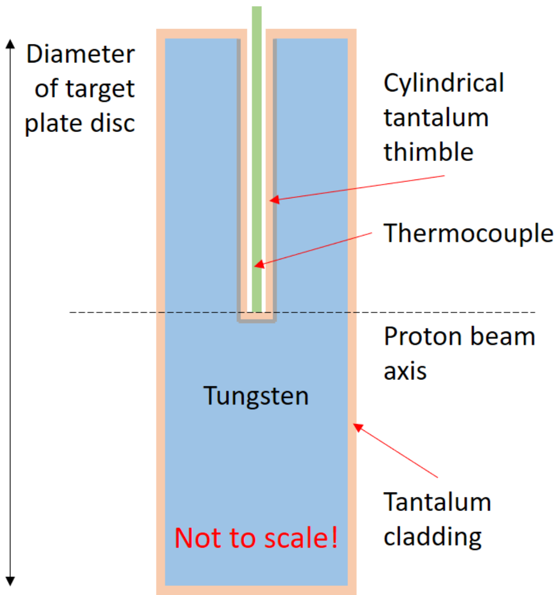

Fig. A1. Sideways section through a plate in the new-style ISIS TS-1 target, *i.e.* looking perpendicular to the axis of the proton beam incident on the target. There is nominally a 0.050-mm gap between the cylindrical thimble and the corresponding cylindrical hole in the plate and a 0.075-mm gap between the thermocouple sheath and the inside of the thimble. The schematic diagram is not to scale, and not all details are shown.

A simple 1-dimensional model of a target plate was set up in the form of a 'cylindrical target plate' including thimble and thermocouple as in the upper part of Fig. A2. In order from the centre ($r = 0$) outwards, the eight radial regions are: chromel/alumel (type-K) thermocouple wires, magnesia (MgO) insulation, stainless steel sheath, very small gap presumably filled with heavy water coolant, tantalum thimble, very thin HIP-ed region (HIP = hot isostatic pressing) between tantalum thimble and surrounding tungsten plate, tungsten, and tantalum cladding. The outer surface was cooled to a thermal sink at 0°C through a heat transfer coefficient of 2.00 W cm^{-2} °C^{-1}. Temperatures T as functions of time t were obtained from the

[5] Much of this appendix is simply a reproduction of the appendix in D J S Findlay, D Wilcox, L Quintieri, G D Howells, D M Jenkins, J D Moor and S D Gallimore, Nucl. Instr. Meth. A 1089 (2026) 171555, https://doi.org/10.1016/j.nima.2026.171555, and is included in the present report simply for readers' convenience.

time-dependent heat equation in cylindrical polar coordinates which was solved starting at $t = 0$ from a uniform temperature of 100°C throughout using the routine DP11 from the Harwell Subroutine Library [20] (integration step lengths of 0.0005 cm and 0.0005 s were used). Values of thermal parameters used are listed in Table A1.

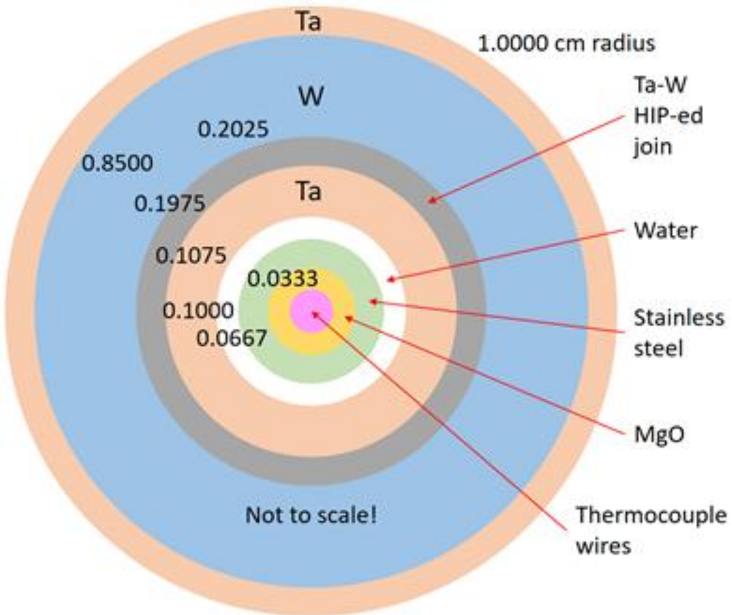

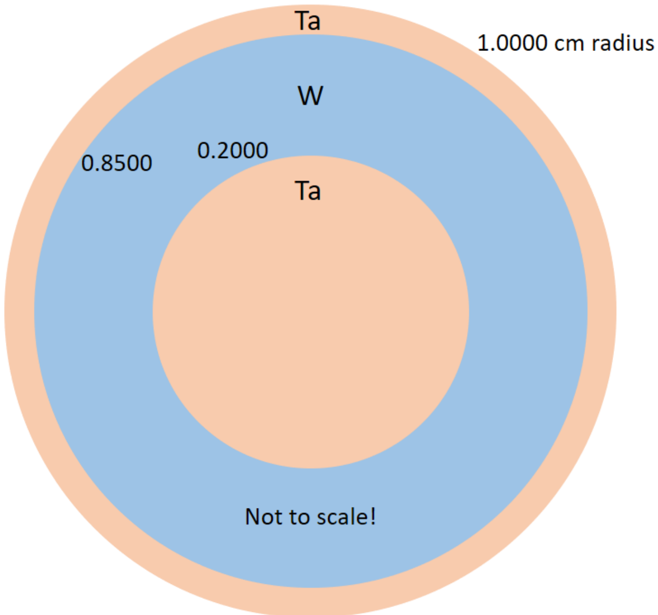

Fig. A2. Upper part (not to scale): cylindrical model of a 2-mm-diameter type-K thermocouple inside a tantalum thimble in a 'cylindrical tungsten target plate'. Lower part (not to scale): same as in the upper part, but with a 'solid tantalum thimble', representing geometry convenient for calculations of temperatures at the centres of plates. These diagrams are intended to represent the essence of the internal structure of a plate viewed from above the top of the plate in Fig. A1. Numbers are radii in centimetres. The internal dimensions of the thermocouple shown are simply plausible estimates.

	Density, g cm^{-3}	Thermal conductivity, W cm^{-1} °C^{-1}	Specific heat, J g^{-1} °C^{-1}	Heat transfer coefficient to thermal sink at 0°C, W cm^{-2} °C^{-1}
Chromel / alumel	8.56	0.26	0.484	
MgO	3.58	0.35	1.03	
Stainless steel	7.8	0.16	0.52	
Heavy water	1.05	0.0063	4.168	
Tantalum	16.6	0.58	0.143	
HIP-ed Ta-W join	17.9	1.105	0.139	
Tungsten	19.2	1.63	0.135	2.00

Table A1. Thermal parameters assumed for model shown in Fig. A2. Data at 100°C mostly from Kaye and Laby [21]. The parameters for the type-K thermocouple wires are the averages of the corresponding parameters for chromel and alumel. The parameters for the HIP-ed join are the averages of the parameters for tantalum and tungsten. Thermal conductivity and specific heat of heavy water from [22] and [23] respectively.

Starting from a uniform 100°C in every region at $t = 0$ when the internal heating is suddenly switched off, decaying temperatures of the eight regions in the upper part of Fig. A2 are shown in Fig. A3. For comparison, Fig. A4 shows the decaying temperatures when the 2-cm-diameter cylinder is wholly composed of tantalum ($0 \leq r < 0.20$ cm), tungsten (0.20 cm $\leq r \leq 0.85$ cm) and tantalum (0.85 cm $< r \leq 1.00$ cm) — *i.e.* the ‘ideal’ three-region assembly of tantalum thimble, tungsten ‘plate’ and tantalum cladding in the lower part of Fig. A2 for which calculated temperatures at the centre of the ‘plate’ are unaffected by any considerations of a thermocouple and its contact with the plate.

As stated in the main text, in order to achieve acceptable fits to measured target plate temperature decays, a smoothing time of ~1 second in the form of a low-pass digital filter had to be included, realised using exponential smoothing. For temperature data $T_i(t_j)$ tabulated in time steps j each of length Δt (0.0005 s in the present work), $T_i^{\mathrm{sm}}(t_j) = \sigma T_i(t_j) + (1-\sigma) T_i^{\mathrm{sm}}(t_{j-1})$ where $T_i^{\mathrm{sm}}(t)$ is the smoothed temperature distribution, $\sigma = 1 - \exp(-\Delta t/\tau_f)$, and τ_f is the time constant of the low-pass filter. Fig. A3 includes smoothed versions of the temperature at the centre of the three-region ideal plate for time constants τ_f of 0.5, 1.0 and 1.5 s. As is evident, the 1.0-s-smoothed curve represents the curve at 0.0167 cm corresponding to the mid-point radius of the thermocouple wires fairly well.

Of course, the modelling of the ‘water gap’ between the stainless-steel sheath of the thermocouple and the inside of the thimble is inherently approximate, as the thermocouple in its sheath is simply a push-fit inside the thimble so that the thermocouple sheath may be touching the inside of the thimble in places, but since actual thermal conductances between thermocouples and thimbles are unlikely ever to be measured, the present calculations do suggest that the 1-second response times of the thermocouples found empirically as described in the main text are not unreasonable.

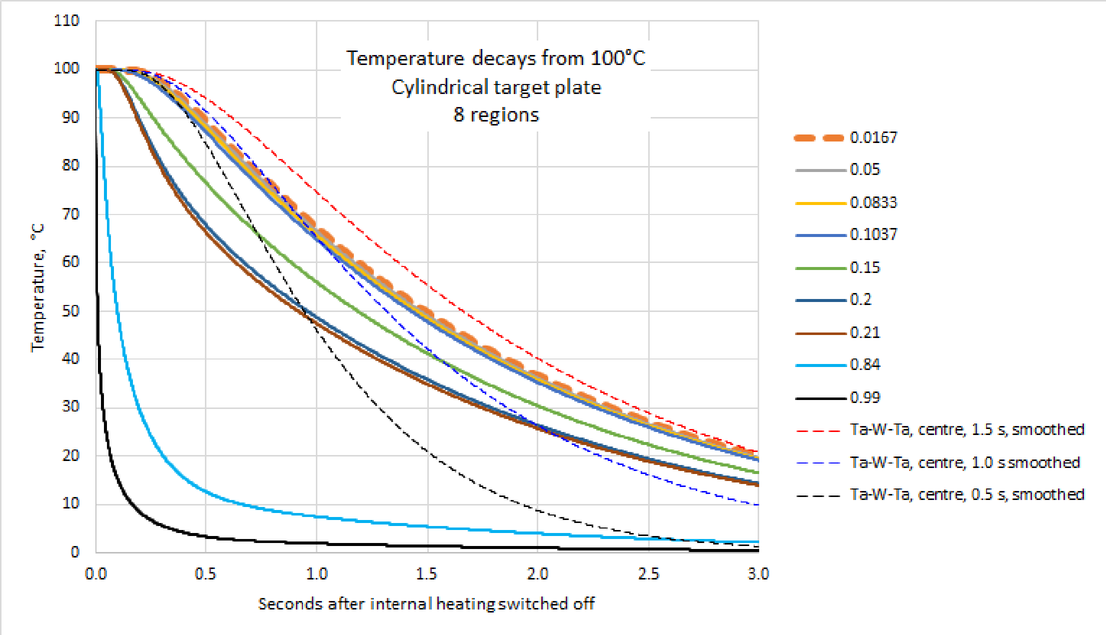

Fig. A3. Solid curves and 0.0167 cm dashed curve: decaying temperatures in the eight regions illustrated in the upper part of Fig. A2. The curves are numbered according to their radial distance r (cm) from the centre, and the 0.0167 cm curve represents the temperature at the mid-point radius of the thermocouple wires. Dashed curves: smoothed versions of the temperature at the centre of the three-region ideal plate for time constants τ_f of 0.5, 1.0 and 1.5 s.

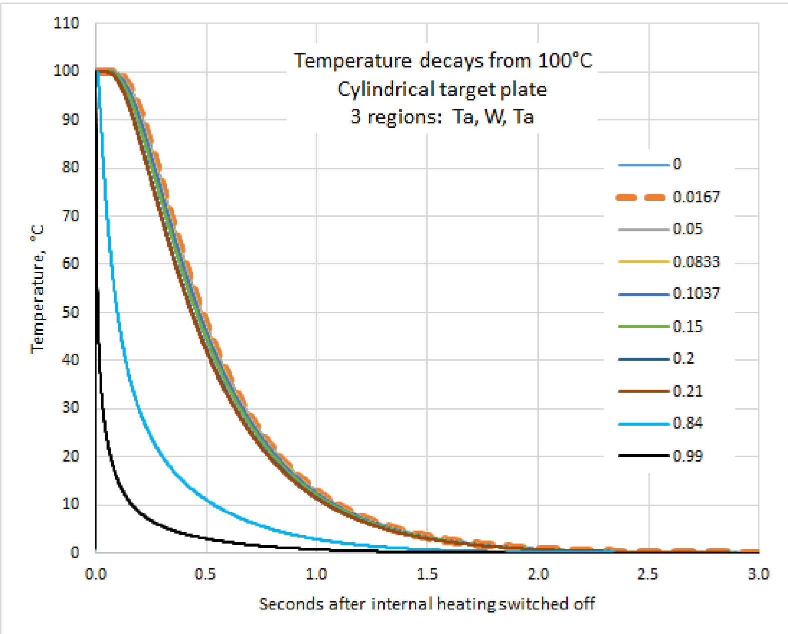

Fig. A4. Decaying temperatures when the eight-region model (Fig. A2, upper) is replaced by a three-region model (Fig. A2, lower) representing an ideal plate as described in the text.

As already stated, the graphs presented in Figs. A3 and A4 are based on the thermophysical parameters listed in Table A1. But what if the thermal conductivities of the materials in the thermocouple itself decrease because of radiation damage? To try to provide some sort of an answer, and in the absence of easily obtainable specific data, the calculations just described were repeated with the thermal conductivities of chromel/alumel, MgO and stainless steel set to half the values in Table A1, and the results are shown in Fig. A5. From the figure, the suggestion could be that the effect of halving the thermal conductivity of each of the three components of the thermocouple (wires, mineral insulation, and sheath) is to increase the time constant by ~0.1–0.2 seconds — although it must be borne in mind that the calculations described in this appendix are full of approximations. and that only a guess has been made at the extent to which the thermal conductivities of materials within the thermocouple are actually affected by irradiation.

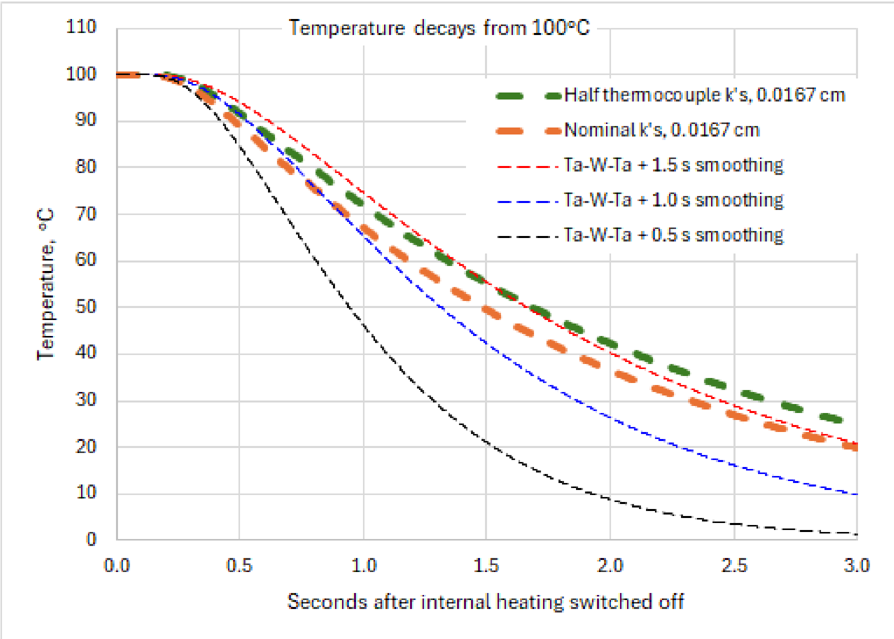

Fig. A5. As Fig. A3, but with the addition of a curve showing the effect of reducing the thermal conductivities of the materials in the thermocouple itself (wires, mineral insulation, and sheath) to half the nominal values listed in Table A1.